arXiv:2303.17185v1 [astro-ph.HE] 30 Mar 2023

Chapter 1
Tests of Classical Gravity with Radio Pulsars

Zexin Hu, Xueli Miao, Lijing Shao

Abstract Tests of gravity are important to the development of our understanding of gravitation and spacetime. Binary pulsars provide a superb playground for testing gravity theories. In this chapter we pedagogically review the basics behind pulsar observations and pulsar timing. We illustrate various recent strong-field tests of the general relativity (GR) from the Hulse-Taylor pulsar PSR B1913+16, the double pulsar PSR J0737−3039, and the triple pulsar PSR J0337+1715. We also overview the inner structure of neutron stars (NSs) that may influence some gravity tests, and have used the scalar-tensor gravity and massive gravity theories as examples to demonstrate the usefulness of pulsar timing in constraining specific modified gravity theories. Outlooks to new radio telescopes for pulsar timing and synergies with other strong-field gravity tests are also presented.

1.1 Introduction

As one of the four fundamental interactions, gravity is the most mysterious to study. From Newton's law of universal gravitation to Einstein's general relativity (GR), in the development of gravity theory, experiments and observations have been playing

Zexin Hu
Department of Astronomy, School of Physics, Peking University, Beijing 100871, China
Kavli Institute for Astronomy and Astrophysics, Peking University, Beijing 100871, China
e-mail: huzexin@pku.edu.cn

Xueli Miao
National Astronomical Observatories, Chinese Academy of Sciences, Beijing 100012, China
e-mail: xlmiao@bao.ac.cn

Lijing Shao (✉)
Kavli Institute for Astronomy and Astrophysics, Peking University, Beijing 100871, China
National Astronomical Observatories, Chinese Academy of Sciences, Beijing 100012, China
e-mail: lshao@pku.edu.cn

an important role in overturning or verifying different gravity theories. Currently, GR has passed all the tests with flying colors [118], and it seems that GR is the *tour de force* among all gravity theories. However, in GR, there is a fundamental difficulty in quantization as well as in describing spacetime singularities, suggesting that GR could not be a complete theory. It might be an effective field theory below some energy scale [113]. So, there is strong motivation to find deviations from GR predictions and to search for other possible alternative gravity theories. People have tried to construct quantum gravity theories to solve the quantization problem in GR, such as the string theory [40]. People have also used alternative gravity theories to explain the missing mass in galaxies and the accelerating expansion of our Universe without introducing the mysterious concepts of dark matter and dark energy [57, 19]. To this end, we need to use all kinds of observations to probe different aspects of gravity and use measurement results to test gravity theories.

People usually classify gravity tests based on the studied systems in different gravity regimes [117, 3, 58]. In astrophysics, for systems of astronomical scales, Wex [117] introduced the following four gravity regimes: (i) quasi-stationary weak-field regime, (ii) quasi-stationary strong-field regime, (iii) highly-dynamical strong-field regime, and (iv) radiation regime. In a quasi-stationary weak-field regime, the velocity of masses is much less than the speed of light c, and spacetime is close to a Minkowski spacetime. Our Solar system belongs to this regime. In a quasi-stationary strong-field regime, the velocity of masses is also much less than c, but one or more masses have strong self-gravity, which causes the neighborhood spacetime to deviate significantly from a Minkowski one. A well-separated binary system containing one or two compact bodies belongs to this regime. In a highly-dynamical strong-field regime, the velocity of masses is close to c and spacetime is strongly curved. The merging of compact binaries reflects the gravity of such a regime. A radiation regime is the propagation regime of gravitational waves (GWs). Gravity tests from the Solar system have provided strict restrictions on the quasi-stationary weak-field regime [118], while the GW detection from LIGO/Virgo/KAGRA probes the radiation regime and provides opportunities to analyze the highly-dynamical strong-field regime [93]. To study the behavior of gravity in a quasi-stationary strong-field regime, we need to have one or more compact bodies in a well-separated system. Binary pulsar systems with good timing precision provide precise measurements of gravity in such a regime.

In this chapter, we will provide a pedagogical introduction to pulsar timing, as well as some aspects and new developments of using it in testing classic (namely, not quantum) gravity theories. In the next section, we overview the basics of pulsar observations and the theoretical background for pulsar timing. We use the famous Hulse-Taylor pulsar PSR B1913+16, the double pulsar PSR J0737−3039, and the triple pulsar PSR J0337+1715 as primary examples for testing GR in Sec. 1.3. After that, we discuss the inner structure of neutron stars (NSs) in Sec. 1.4 which in some theories will affect the binary orbital dynamics. A couple of representative alternative gravity theories are tested against pulsar timing data in Sec. 1.5. Finally, Sec. 1.6 summaries the chapter. More reviews on the topic of using radio pulsars for gravity tests can be found in Refs. [106, 117, 78, 100, 97, 58].

1.2 Pulsar Observation and Pulsar Timing

In 1967, the first pulsar PSR B1919+21 was discovered [50]. The prevailing view of pulsars is that they are stably spinning NSs with a high-intensity magnetic field [45]. In a pulsar's open magnetic field line region, the charged particles moving along magnetic field lines can produce curvature radiation, creating a radiation cone centered on the magnetic axis [73]. Generally, a pulsar's magnetic axis and spin axis do not coincide, so if the radiation region of a NS sweeps past Earth's radio telescopes when the NS rotates, one can detect a series of periodic pulse signals on the Earth. In this setting, a rotating NS seems like a lighthouse, that is why we also call it the "lighthouse model." Pulsars, as rapidly rotating NSs, provide an ideal laboratory in astrophysics for fundamental physics. The masses of NSs are typically larger than that of our Sun, but their radii are only about 10 km. Therefore NSs represent an extremely dense stellar environment. Inside NSs there exists high matter density, which can reach and exceed nuclear density, $\sim 10^{15}\,\mathrm{g/cm^3}$, as well as high pressure, $\sim 10^{36}\,\mathrm{erg/cm^3}$. NSs also have high magnetic field ranging from $10^8\,\mathrm{G}$ to $10^{15}\,\mathrm{G}$.

Benefiting from the development of telescopes, we have detected more than 3000 pulsars up to now. Figure 1.1 shows the population of pulsars by the distribution of spin period (P) and spin period derivative ($\dot{P}$) [79]. In the figure the red circle marks pulsars in binary systems, which make up about 10% of detected pulsars. These pulsars' spin periods range from 1.4 ms to 24 s. According to the distribution of P and $\dot{P}$, one can classify pulsars into two groups: normal pulsars which correspond to the distribution in the upper right part in Fig. 1.1, and millisecond pulsars (MSPs) which correspond to the distribution in the bottom left part. For MSPs, as the name suggests, the spin periods are mostly less than 10 ms and the spin period derivatives range from $10^{-18}\,\mathrm{s\,s^{-1}}$ to $10^{-22}\,\mathrm{s\,s^{-1}}$. The small $\dot{P}$ of MSPs means that they have more stable spin periods than normal pulsars on long timescales, and the stability of some MSPs can revive the precision of atomic clocks in long timescales [72, 79, 53]. The fast rotation of MSPs is caused by the "recycling process" where the pulsars can spin up by a stable mass transfer from the companion stars [108]. So, MSPs are mostly found in binary systems, as clearly seen in Fig 1.1. Fully recycled pulsars would have millisecond spin periods and locate in very circular orbits. Some pulsars could undergo mild recycling processes and only spin up to $\gtrsim 10$ ms, and their orbits would be eccentric. The stability of spin periods of MSPs makes the measurements of them highly precise. As discussed earlier, the motion of a MSP in a binary system probes the quasi-stationary strong-field regime of gravity. So detecting a stably rotating MSP in a binary system allows us to test gravity in a quasi-stationary strong-field regime.

The radiation of a pulsar can be detected in multiple frequency bands. For example, the Crab pulsar, a young pulsar discovered in the Crab nebula, radiates pulses from the radio bands to γ-ray bands [105, 75]. The discovery of the Crab pulsar in the Crab nebula also demonstrates that a rotating NS is a product of a supernova. While other bands also provide important information, study of pulsars is mainly benefited from the radio band. Pulsars usually have a power-law radio spectrum and the spectrum index is normally from -2 to -1.5 [73].

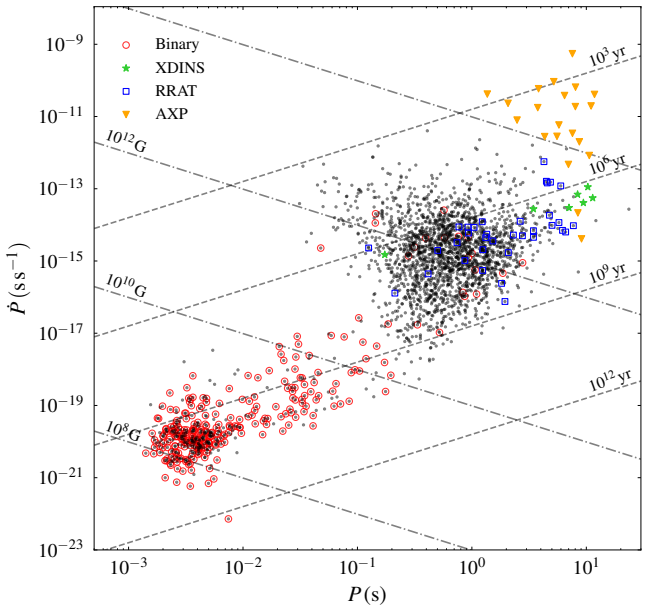

Fig. 1.1: The period–period derivative diagram for pulsars [79]. The black dots are pulsars with pulsed emission in the radio band and the red circles mark binary systems. We also denote "AXP" for systems that are anomalous X-ray pulsars or soft γ-ray repeaters, "RRAT" for systems that are pulsars with intermittently pulsed radio emission, and "XDINS" for systems that are isolated NSs with pulsed thermal X-ray emission but no detectable radio emission.

The pulse radiation passes through the ionized interstellar medium (ISM) before being detected by radio telescopes. The ISM causes radio signals to disperse in the propagation, so the timing of the signal is frequency dependent. For signal of frequency f, the time delay t caused by ISM follows $t = D \times \mathrm{DM}/f^2$, namely that the signals of higher frequency arrive earlier than those of lower frequency. The parameter $D \equiv e^2/2\pi m_e c = (4148.808 \pm 0.003)\,\mathrm{MHz^2\,pc^{-1}\,cm^3\,s}$ is the dispersion constant, where e and m_e are the charge and mass of an electron respectively. "DM" is the dispersion measure, which controls the magnitude of the delay, defined via $\mathrm{DM} \equiv \int_0^d n_e \mathrm{d}l$, where d is the distance of the pulsar and n_e is the electron number density. Using the time delay between two different frequencies (f_1 and f_2),

$$\Delta t = D \times \left(f_1^{-2} - f_2^{-2}\right) \times \mathrm{DM}\,, \tag{1.1}$$

we can calculate the value of DM. With a Galactic electron density distribution model, we can calculate the distance of the pulsar. There are two mainstream models, the NE2001 model [20] and the YMW model [127]. As post processing for

the observation, to rectify the dispersion effect during propagation, one can adopt "incoherent dedispersion" or "coherent dedispersion" techniques.

In reality, the ISM is highly turbulent and inhomogeneous, and the irregularity induces extra effects on the propagating signals. It causes multi-path scattering of the radio signals, leading pulse profiles of pulsars to have "exponential tails" which blur the profile edges and worsen the timing precision. The scattering effect decreases with frequency roughly as f^{-4}, so using a higher frequency band to observe reduces the scattering effect [73]. In addition, the relative motion between the pulsar, the scattering screen, and the radio telescope can cause interstellar scintillation. It leads to intensity variations of the pulsar's signals on various timescales and frequencies [73].

After accounting for the dispersion effects of pulse signals, we get a series of single pulses. Figure 1.2 shows 100 continuous single pulses versus spin phase from PSR J2222−0137, which was observed by the Five-hundred-meter Aperture Spherical radio Telescope (FAST). In the figure, the pulse-to-pulse variation of profiles is not stable. Generally, the profiles of single pulses of a pulsar are stochastic. But some pulsars exhibit unique temporal characteristics, such as sub-pulse drifting [37, 115], mode changing [8], nulling [6, 112], giant pulse [105, 48], and microstructures [21]. The investigation of pulsars' single pulses helps one reveal the radiation mechanism of pulsars and the structure of the emission region. Here we do not provide a detailed introduction on the single-pulse study, more relevant studies on this topic can be found in Refs. [95, 70]. We will concentrate on introducing the pulsar timing technique that helps us measure pulsars' physical properties.

For pulsar timing, we measure the times of arrival (TOAs) of a pulsar's radio signals at radio telescopes on the Earth and use a timing model to fit the TOAs to get a phase-connection solution [30, 117]. To generate TOAs, we should use pulse profiles to cross correlate with the "standard profile" of the pulsar at that observing frequency. To achieve high-precision TOAs, we need to use stable profiles of pulses. The shape of profiles is highly variable from pulse to pulse. The integration of hundreds or thousands of pulse periods leads to stable profiles. In addition, except for bright pulsars, single pulses of a pulsar are faint, and it is difficult to detect single pulses. So, to get a stable profile with a high signal-to-noise ratio (SNR), we need to fold hundreds or thousands of pulse signals according to a pulsar's spin period. In Fig. 1.2, the profile in the top is the integrated profile of PSR J2222−0137, and it is folded from the 100 single pulses. Generally, we cannot simply get the spin period directly from the pulse TOA intervals. The propagation effects on signals and the motion of pulsars cause various time delays to TOAs. We need to adopt a specific timing model to predict these time-delay effects and get the intrinsic rotation periods.

The intrinsic rotation frequency of a pulsar can be Taylor-expanded by [30, 73],

$$\nu(T) = \nu_0 + \dot{\nu}_0 (T - t_0) + \frac{1}{2}\ddot{\nu}_0 (T - t_0)^2 + \cdots , \tag{1.2}$$

where T is pulsar proper time, $\nu_0 \equiv \nu(t_0)$ is the spin frequency at reference epoch t_0, $\dot{\nu}_0$ and $\ddot{\nu}_0$ are the first and second time derivatives of spin frequency at t_0. In the

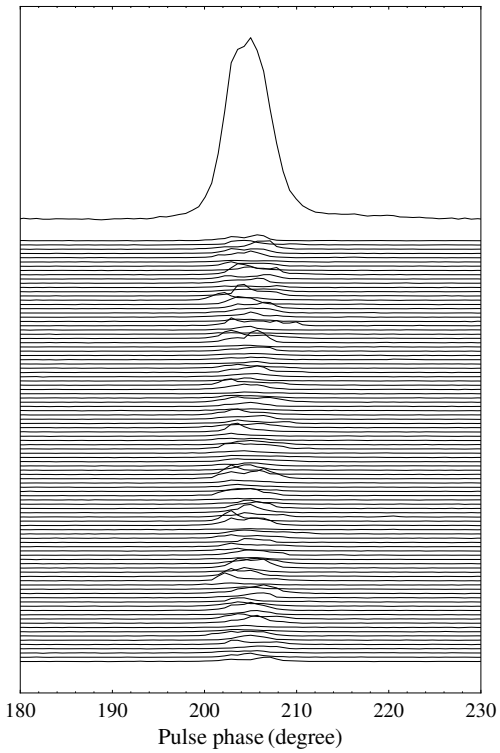

Fig. 1.2: Stack of 100 single pulses from PSR J2222−0137, observed with the FAST telescope. The line in the top is the integrated profile of these 100 pulses.

magnetic dipole model, the radiation of a pulsar takes away the rotation energy and makes the pulsar spin down, which contributes to $\dot{\nu}_0$ and $\ddot{\nu}_0$. We can also rewrite Eq. (1.2) as the relation between the pulsar's proper time and pulse number N [30],

$$N = N_0 + \nu_0 (T - t_0) + \frac{1}{2}\dot{\nu}_0 (T - t_0)^2 + \frac{1}{6}\ddot{\nu}_0 (T - t_0)^3 + \cdots . \tag{1.3}$$

Equations (1.2) and (1.3) describe the pulsar rotation in a reference frame co-moving with the pulsar. For us, what we measure is TOAs of pulses recorded by an atomic clock on the Earth. The recorded TOAs are in the non-inertial frame of reference where the radio telescope is located. So we need to translate the TOAs to an inertial frame, and the Solar System Barycentre (SSB) is an excellent approximate inertial reference frame. For a solitary pulsar, its proper time T equals to its time at SSB of infinite frequency up to a constant. It can be expressed by [30],

$$T = t_{\rm tele} + t_c - \frac{D \times \mathrm{DM}}{f^2} + \Delta_{\mathrm{R}_\odot} + \Delta_{\mathrm{S}_\odot} + \Delta_{\mathrm{E}_\odot} , \tag{1.4}$$

where $t_{\rm tele}$ is the time that a pulse arrivals at a telescope, t_c is the relative correction between an atomic clock of the telescope to an average reference clock, $D \times {\rm DM}/f^2$ is the correction of dispersion effect, f is the observing frequency, $\Delta_{\rm R_\odot}$ is the Römer delay caused by the motion of the Earth around the Sun, $\Delta_{\rm S_\odot}$ is the Shapiro delay which is a relativistic delay from the curvature of spacetime caused by the presence of masses in the Solar system (notably the Sun and the Jupiter), $\Delta_{\rm E_\odot}$ is the Einstein delay which is a combined effect of gravitational redshift caused by masses in the Solar system and time dilation caused by the motion of the Earth.

In gravity tests with radio pulsars, binary pulsar systems are the main objects of investigation. For a pulsar in a binary system, the orbital motion of the pulsar and the gravity field of the companion lead to extra time delays. For binary pulsar systems, Eq. (1.4) is extended to [30],

$$T = t_{\rm tele} + t_c - \frac{D \times {\rm DM}}{f^2} + \Delta_{\rm R_\odot} + \Delta_{\rm S_\odot} + \Delta_{\rm E_\odot} + \Delta_{\rm RB} + \Delta_{\rm SB} + \Delta_{\rm EB} + \Delta_{\rm AB}\,. \quad (1.5)$$

Compared with Eq. (1.4), it has four additional terms: $\Delta_{\rm RB}$ is the Römer delay caused by the orbital motion of the pulsar; $\Delta_{\rm SB}$ is the Shapiro delay caused by the gravity field of the companion star in the binary; $\Delta_{\rm EB}$ is the Einstein delay which is caused by the time dilation and gravitational redshift, and they are due to the orbital motion of the pulsar; $\Delta_{\rm AB}$ is the aberration delay that results from aberration of the rotating pulsar beam, and this effect depends on the time-varying transverse component of the orbital velocity of the pulsar [73].

The motion of a pulsar in a binary orbit can be described by six Keplerian parameters, and they are the orbital period of the pulsar P_b, the orbital eccentricity e, the projected semi-major axis x, the longitude of periastron relative to the ascending node ω, the time of periastron passage T_0, and the position angle of the ascending node $\Omega_{\rm asc}$ which we generally cannot measure solely from pulsar timing unless the binary pulsar is very nearby [73]. When the six Keplerian parameters are determined, we can describe the motion of a binary system well. However, these parameters change with time because of various reasons. For example, for a binary pulsar system, the pulsar and the companion are slowly inspiraling and the system radiates GWs outward. So we need to consider orbital evolution over time.

After the first binary pulsar system PSR B1913+16 was detected [56], how to provide a simple timing model with correct binary motion became a hot topic that was constantly discussed at that time. Considering the first-order post-Newtonian (PN) approximation and combining with the pulsar observational data, Damour and Deruelle [23, 24] proposed a phenomenological parametrization—the so-called parametrized post-Keplerian (PPK) formalism—and later Damour and Taylor [30] extended it. The PPK parameters reflect orbital effects beyond the Keplerian orbit that can be extracted from pulsar timing and do not depend on specific boost-invariant gravity theories at the 1 PN order. The Damour-Deruelle (DD) timing model gets the orbital motion information by fitting a series of Keplerian and PPK parameters. The commonly used observable PPK parameters are [24, 30],

$$\{p^{\rm PPK}\} = \{\dot{\omega}, \gamma, \dot{P}_b, r, s, \delta_\theta\}\,, \quad (1.6)$$

where $\dot{\omega}$ is the advance rate of periastron, $\dot{P}_b$ is the decay rate of orbital period, γ is the amplitude of $\Delta_{\rm EB}$, r and s are the PPK parameters describing $\Delta_{\rm SB}$, δ_θ is a PPK parameter in $\Delta_{\rm RB}$.

Considering GW radiation makes orbital parameters change with time. Based on the Kepler's equation, Damour and Deruelle [23, 24] provided a Kepler-like equation,

$$u - e\sin u = \frac{2\pi}{P_b}\left[(T-T_0) - \frac{\dot{P}_b}{2}\frac{(T-T_0)^2}{P_b}\right], \tag{1.7}$$

where u is the eccentric anomaly, and its relation to the true anomaly $A_e(u)$ is,

$$A_e(u) = 2\arctan\left[\sqrt{\frac{1+e}{1-e}}\tan\frac{1}{2}u\right]. \tag{1.8}$$

The longitude of periastron ω can be modified as, $\omega = \omega_0 + \dot{\omega}A_e(u)/n_b$, where $n_b = 2\pi/P_b$ is the average angular velocity of the orbit.

Damour and Deruelle [24] provided the time delay terms for binary systems. The Römer delay is,

$$\Delta_{\rm RB} = x\sin\omega\left[\cos u - e\left(1+\delta_r\right)\right] + x\left[1-e^2\left(1+\delta_\theta\right)^2\right]^{1/2}\cos\omega\sin u, \tag{1.9}$$

where δ_r is also a PPK parameter, but we cannot get it by directly fitting it in the timing model, because it can be absorbed by redefining other parameters. δ_θ and δ_r describe the relativistic deformations of the orbit. Damour and Deruelle used three eccentricities, and the two new eccentricities are defined via $e_{\rm r} \equiv e\left(1+\delta_{\rm r}\right)$ and $e_\theta \equiv e\left(1+\delta_\theta\right)$.

The Einstein delay of a binary is,

$$\Delta_{\rm EB} = \gamma\sin u, \tag{1.10}$$

where γ represents the amplitude combining time dilation and gravitational redshift. The Einstein delay is degenerate with the Römer delay, and the degree of degeneracy depends on the change of ω [30], namely, if ω changes significantly, the degeneracy can be broken.

The Shapiro delay of a binary is [12],

$$\Delta_{\rm SB} = -2r\ln\left\{1 - e\cos u - s\left[\sin\omega(\cos u - e) + \left(1-e^2\right)^{1/2}\cos\omega\sin u\right]\right\}, \tag{1.11}$$

where r and s are the above-mentioned range and shape parameters respectively. The Shapiro delay effect will be noticeable when the orbital inclination i, which is the inclination of the orbit with respect to the line of sight, is close to 90°, that is, the binary system is close to edge-on. Otherwise, this effect can be partially absorbed in other timing parameters. A strong Shapiro delay effect provides a direct measurement of the mass of the companion and the inclination angle i. For low-eccentricity binary systems, the PPK parameters r and s have a high correlation, especially when

the inclination angle i is not sufficiently close to 90°. In this situation, we cannot get r and s with high precision. Freire and Wex [41] provided two new PPK parameters, h_3 and h_4, to alleviate this problem. The PPK parameters h_3 and h_4 are the amplitudes of the third and fourth harmonics from the Shapiro delay's Fourier expansion. Compared with r and s, h_3 and h_4 are less correlated with each other. For edge-on systems, parameters h_3 and ζ are introduced to replace h_3 and h_4, where $\zeta \equiv h_3/h_4$ is the ratio of amplitudes of successive harmonics. The parameters h_3 and ζ provide a superior description of the constraints on the orbital inclination i and the masses of the binary than r and s. In the new parametrization, the Shapiro delay is rewritten as [41],

$$\Delta_{\rm SB} = -\frac{2h_3}{\zeta^3}\ln\left(1+\zeta^2-2\zeta\sin\Phi\right), \tag{1.12}$$

where Φ is the longitude relative to the ascending node. The relations between (h_3, ζ) and (s, r) are $s = 2\zeta/(\zeta^2+1)$ and $r = h_3/\zeta^3$ [41].

Finally, the aberration delay is [73],

$$\Delta_{\rm AB} = A\left\{\sin\left[\omega + A_e(u)\right] + e\sin\omega\right\} + B\left\{\cos\left[\omega + A_e(u)\right] + e\cos\omega\right\}, \tag{1.13}$$

where A and B are both PPK parameters, but they are not separately measurable by pulsar timing.

After considering these time delay terms contributed to the timing model, we can precisely measure orbital parameters by pulsar timing. For boost-invariant gravity theories, in the DD timing model, the PPK parameters are functions of Keplerian parameters, masses of the binary and parameters of gravity theories. In GR, PPK parameters are functions of Keplerian parameters and masses of the binary only. In GR, PPK parameters in Eq. (1.6) are expressed as [73, 117],

$$\dot{\omega} = \frac{3n_b}{1-e^2}\frac{V_b^2}{c^2}, \tag{1.14}$$

$$\gamma = \frac{e}{n_b}\left(1+\frac{m_c}{m}\right)\frac{m_c}{m}\frac{V_b^2}{c^2}, \tag{1.15}$$

$$r = \frac{Gm_c}{c^3}, \tag{1.16}$$

$$s = \sin i = x n_b \frac{m}{m_c}\frac{c}{V_b}, \tag{1.17}$$

$$\delta_\theta = \frac{(7/2)m_p^2 + 6m_p m_c + 2m_c^2}{m^2}\frac{V_b^2}{c^2}, \tag{1.18}$$

$$\dot{P}_b = -\frac{192\pi}{5}\frac{m_p m_c}{m^2} f(e)\frac{V_b^5}{c^5}, \tag{1.19}$$

where $V_b \equiv (Gmn_b)^{1/3}$ and $f(e) = \left[1+(73/24)e^2+(37/96)e^4\right](1-e^2)^{-7/2}$. In the above equations, m_p is the mass of the pulsar, m_c is the mass of the companion, m

is the total mass of the binary and $x \equiv a_p \sin i/c$ is the projected semi-major axis of pulsar's orbit in the unit of seconds.

In relativistic gravity theories, the spins of the bodies that orbit in a binary system can affect their orbital and spin dynamics. Three contributions are induced by a rotating body moving in a binary pulsar system at the leading orders. They are the spin-orbit interaction between the spin of pulsar $\mathbf{S}_p$ and the orbital angular momentum $\mathbf{L}$, the spin-orbit interaction between the spin of companion $\mathbf{S}_c$ and $\mathbf{L}$, and the spin-spin interaction between $\mathbf{S}_p$ and $\mathbf{S}_c$ [117]. The spin-spin interaction is generally many orders of magnitude smaller than the 2 PN terms and the spin-orbit effects, so that one can ignore it. We only introduce the spin-orbit interaction here. In a binary pulsar system, the spin-orbit interaction leads the orbit and the two spins to precess [117, 7]. The main effect of the precession of the spin is a secular change in the orientation of the spin, which is caused by the effect of spacetime curvature and the precessing rate is independent of the spin. This effect is the so-called geodetic precession, and it has been detected in some binary pulsar systems, such as PSR J0737−3039 [15] and PSR J1906+0746 [32].

For a pulsar in a binary system, geodetic precession causes the pulsar's spin to precess around the total angular momentum. As the orbital angular momentum is normally much larger than the pulsar's spin, we can regard that the pulsar's spin precesses around the orbital angular momentum. In GR, the average rate of geodetic precession of the pulsar's spin at the leading order is [73],

$$\Omega_p = \frac{n_b}{1-e^2}\left(2+\frac{3m_c}{2m_p}\right)\frac{m_p m_c}{m^2}\frac{V_b^2}{c^2}\,. \tag{1.20}$$

The secular change of the spin orientation causes changes in the observed emission properties of the pulsar because the line-of-sight will cut through different regions of the magnetosphere. One can detect a changing integrated profile and polarization angle (PA) in data. In turn, one can use the change of profile or PA to calculate Ω_p, and compare the results with GR's predictions [32].

The orbital precession has two effects that need to be considered. The first effect is due to the mass-mass interaction, which belongs to the PN terms of two point masses. The second effect is due to the Lense-Thirring effect related to the spins of two stars [7]. Damour and Schaefer [29] decomposed the precession of the orbit in terms of observable parameters of pulsar timing. One of the parameters is $\dot{\omega}_p$, which can be decomposed into,

$$\dot{\omega}_p = \dot{\omega}_{\rm PN} + \dot{\omega}_{{\rm LT}_p} + \dot{\omega}_{{\rm LT}_c}\,, \tag{1.21}$$

where $\dot{\omega}_{\rm PN}$ is the PN term and the 1 PN order is given in Eq. (1.14); $\dot{\omega}_{{\rm LT}_p}$ and $\dot{\omega}_{{\rm LT}_c}$ are due to the Lense-Thirring effect of the pulsar and the companion respectively. For a binary NS system, the spin of the companion is generally slow, so the $\dot{\omega}_{{\rm LT}_c}$ that comes from the contribution of the companion's spin can be ignored. If $\mathbf{S}_p$ is parallel to the orbital angular momentum $\mathbf{L}$, the $\dot{\omega}_{{\rm LT}_p}$ can be simplified to [7, 54],

$$\dot{\omega}_{\mathrm{LT}_p} = -\frac{3n_b}{1-e^2}\beta_p^{\mathrm{s}} g_{p\parallel}^{\mathrm{s}} \frac{V_b^3}{c^3}\,, \tag{1.22}$$

where $X_p \equiv m_p/m$, $\beta_p^{\mathrm{s}} \equiv cI_p n_b/Gm_p^2$, $g_{p\parallel}^{\mathrm{s}} \equiv \left(\frac{1}{3}X_p^2 + X_p\right)\left(1-e^2\right)^{-1/2}$, and I_p is the moment of inertia of the pulsar which depends on the equation of state (EOS) of NSs. As we can see, the value of $\dot{\omega}_{\mathrm{LT}_p}$ depends on I_p. So if we can measure $\dot{\omega}_{\mathrm{LT}_p}$, we can get a value of I_p which can help us determine the EOS of NSs. However, using the best-measured double pulsar as an example [61, 54, 60], the value of $\dot{\omega}_{\mathrm{LT}_p}$ is at the same order as the value of $\dot{\omega}_{2\,\mathrm{PN}}$, so only highly relativistic binary pulsar systems with high-precision timing results might have the ability to limit the moment of inertia of NSs with this method.

1.3 Hulse-Taylor Pulsar, Double Pulsar, and Triple Pulsar

With the theoretical background in the last section, we now introduce three of the most famous radio pulsars in the field, the Hulse-Taylor pulsar PSR B1913+16 [56, 109, 114], the double pulsar PSR J0737−3039A/B [16, 76, 59, 15, 60], and the triple pulsar PSR J0337+1715 [87, 5, 111].

1.3.1 The first binary pulsar: PSR B1913+16

PSR B1913+16, a recycled pulsar in a highly eccentric 7.75-hr orbit, was the first pulsar detected in a binary system. The binary is a double NS system, and it was discovered using the Arecibo telescope in 1974 [56]. We also call this pulsar the Hulse-Taylor pulsar in honor of its discoverers. The discovery of this system indirectly proved the existence of GW radiation for the first time [109]. The latest timing results of this pulsar are published in Ref. [114], where 9257 TOAs were acquired over 35 years, and the analysis provided stringent tests of gravity theories. The orbital parameters in DD timing model are listed in Table 1.1. Three PPK parameters—the advance rate of periastron $\dot{\omega}$, the amplitude of Einstein delay γ, and the decay rate of orbital period $\dot{P}_b$—were well determined [114]. In addition, two PPK parameters, r and s, of the Shapiro delay effect from this system were measured. All these measurements are consistent with GR predictions. The relativistic shape correction to the elliptical orbit, $\delta_\theta^{\mathrm{obs}}$, is also detected for the first time.

Assuming GR is the true theory of gravity, Eqs. (1.14–1.15) were used to get the masses of the binary, $m_p = 1.438 \pm 0.001\,M_\odot$ and $m_c = 1.390 \pm 0.001\,M_\odot$ [114]. Inserting the measured Keplerian parameters and the derived masses into Eq. (1.19), Weisberg and Huang [114] got a theoretical prediction in GR, $\dot{P}_b^{\mathrm{GR}} = -(2.40263 \pm 0.00005) \times 10^{-12}$. Table 1.1 shows the value of the observed decay rate of orbital period $\dot{P}_b^{\mathrm{obs}}$, and it must be corrected by terms $\dot{P}_b^{\mathrm{Shk}}$, the dynamical contributions from the Shklovskii effect and $\dot{P}_b^{\mathrm{Gal}}$, the differential Galactic acceleration between

Table 1.1: Orbital parameters of PSR B1913+16 [114].

Parameter	Value
$x = a_p \sin i/c$ (s)	2.341776(2)
e	0.6171340(4)
P_b (d)	0.322997448918(3)
ω_0 (deg)	292.54450(8)
$\dot{\omega}$ (deg yr^{-1})	4.226585(4)
γ (ms)	0.004307(4)
$\dot{P}_b^{\rm obs}$	$-2.423(1)\times10^{-12}$
$\delta_\theta^{\rm obs}$	$4.0(25)\times10^{-6}$
s	$0.68^{+0.10}_{-0.06}$
r (μs)	$9.6^{+2.7}_{-3.5}$
ζ	0.38(4)
h_3 (s)	$0.6(1)\times10^{-6}$

the SSB and the pulsar system. After subtracting the total contribution from $\dot{P}_b^{\rm Shk}$ and $\dot{P}_b^{\rm Gal}$, $-(0.025\pm0.004)\times10^{-12}$, an intrinsic value is obtained, $\dot{P}_b^{\rm intr} = -(2.398\pm0.004)\times10^{-12}$ [114]. Using $\dot{P}_b^{\rm GR}$ and $\dot{P}_b^{\rm intr}$, Weisberg and Huang found that the ratio of the observed orbital period decrease caused by the GW damping to its GR prediction is [114],

$$\frac{\dot{P}_b^{\rm intr}}{\dot{P}_b^{\rm GR}} = \frac{-(2.398\pm0.004)\times10^{-12}}{-(2.40263\pm0.00005)\times10^{-12}} = 0.9983\pm0.0016\,. \tag{1.23}$$

This result provided the most precise test of GW emission in 2016. One can notice that the uncertainty of $\dot{P}_b^{\rm intr}$ is dominated by the errors of $\dot{P}_b^{\rm Shk}$ and $\dot{P}_b^{\rm Gal}$, which depend on the precision of the pulsar distance measurement and the Galactic acceleration model.

As mentioned above, assuming GR is correct and using the measured two PPK parameters, one can get m_p and m_c. If one measures three or more PPK parameters, one can do self-consistency checks in GR. Mass-mass diagram illustrates the self-consistency checks. Using Eqs. (1.14–1.19), one can plot the m_p-m_c curves for each observed PPK parameter and check whether they intersect at a common region within measurement uncertainties. Figure 1.3 shows the mass-mass diagram of PSR B1913+16 [114], and the curves of five PPK parameters all meet within measurement uncertainties. For PSR B1913+16, three PPK parameters, $\dot{\omega}$, γ and $\dot{P}_b^{\rm intr}$, are measured with high precision; the 1-σ errors of them are smaller than the widths of the curves in the figure. All lines intersect in a tiny region, which provides a strict test of GR in the strong-field condition.

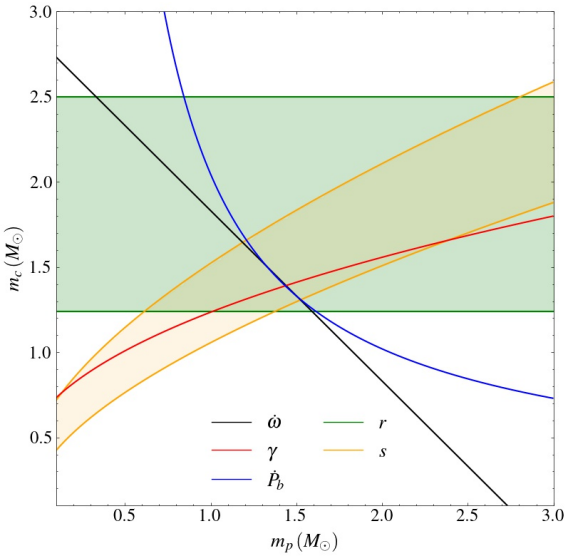

Fig. 1.3: Mass-mass diagram of PSR B1913+16 [114], assuming that GR is right and using the five PPK parameters listed in Table 1.1. The width of each band represents the ± 1-σ uncertainty. For $\dot{\omega}$, γ and $\dot{P}_b^{\rm intr}$, the uncertainties of them are smaller than the widths of the lines. The intersection of all bands is consistent within a small region, which illustrates the agreement of the observations with GR.

1.3.2 The double pulsar system: PSR J0737−3039A/B

PSR J0737−3039A/B, discovered in 2003, is currently the only known double pulsar system in which both NSs are detectable as radio pulsars [16]. PSR J0737−3039A is a 22.7-ms MSP pulsar which was first-born and spun up by accreting materials from the companion; PSR J0737−3039B is the second-born pulsar with $P = 2.7\,$s and, due to the geodetic precession, its radio emission disappeared in 2008 [15]. The two pulsars orbit each other in a mildly eccentric ($e = 0.088$) orbit with $P_b = 2.45\,$hr [76, 59]. The double pulsar system's orbital period is only one-third of that of the Hulse-Taylor pulsar, which means PSR J0737−3039A/B has a higher average orbital velocity and a larger acceleration. So it is a more relativistic binary system and an excellent testbed for strong-field gravity when well timed.

In 2006, Kramer et al. [59] reported 2.5-yr timing results of PSR J0737−3039A/B, which provided four independent strong-field tests of GR. Although only using 2.5 years of timing data, because of the larger relativistic effect in this system, the PPK parameters $\dot{\omega}$, γ and $\dot{P}_b$ were already well measured. The orbit is nearly edge-on, so the PPK parameters r and s of the Shapiro delay effect also have precise measurements. Because the two pulsars' emissions are detectable for this system, the projected semi-major orbital axes $x_{\rm A}$ and $x_{\rm B}$ are both measured with high preci-

Table 1.2: Four independent tests of GR provided by the PPK parameters of the double pulsar [59]. The last column shows the ratios of observed values to their expectation in GR.

PPK Parameter	Observed	Expected in GR	Ratio
$\dot{P}_b$ (10^{-12})	$-1.252(17)$	$-1.24787(13)$	1.003(14)
γ (ms)	0.3856(26)	0.38418(22)	1.0036(68)
s	$0.99974(-39,+16)$	$0.99987(-48,+13)$	0.99987(50)
r (μs)	6.21(33)	6.153(26)	1.009(55)

sion. Therefore this system provides an accurate measurement of the mass ratio $R = m_{\rm A}/m_{\rm B} = x_{\rm B}/x_{\rm A}$, which is a theory-independent parameter in boost-invariant gravity theories. Kramer et al. [59] used the most precisely measured PPK parameter $\dot{\omega} = 16.89947(68)\,\deg\,{\rm yr}^{-1}$ and the theory-independent parameter $R = 1.0714(11)$ to derive the masses of the binary, $m_{\rm A} = 1.3381(7)\,M_\odot$ and $m_{\rm B} = 1.2489(7)\,M_\odot$. The masses are then used to calculate the theoretical values of other PPK parameters with the assumption that GR is right. In Table 1.2 we show the results of four independent gravity tests. The fourth column is the ratio of observed values to their expectation in GR, wherein the ratio for s was the best available Shapiro-delay test of GR in the strong-field region at that time. With only 2.5-yr data, it reveals PSR J0737−3039A/B's outstanding ability to test GR.

For PSR J0737−3039A/B, it shows a roughly 30-s eclipse when pulsar A passes behind pulsar B, namely, pulsar A is at the superior conjunction of its orbit. Pulsar A's pulse signals will be absorbed by the magnetosphere of pulsar B when the eclipse happens. For pulsar B, the misalignment angle between the spin vector and the total angular momentum vector is significant, $\delta_B \simeq 50^\circ$, leading to a measurable geodetic precession of pulsar B's spin, $\mathbf{S}_B$. The geodetic precession of $\mathbf{S}_B$ causes a changing absorption effect at the eclipse. Breton et al. [15] used a simple geometric model to characterize the observed changing eclipse morphology and measured the geodetic precession of $\mathbf{S}_B$ around the total orbital angular momentum. They got a relativistic spin precession rate, $\Omega_B = 4.77^\circ(+0.66^\circ, -0.65^\circ)\,{\rm yr}^{-1}$, and this result is consistent with the value, $\Omega_B^{\rm GR} = 5.0734(7)^\circ\,{\rm yr}^{-1}$, predicted by GR, providing a new test of GR in the strong-field regime [15].

In 2021, Kramer et al. [60] reported 16.2-yr timing data of the double pulsar observed with six radio telescopes. These results show an excellent ability to test gravity theories because they not only provide very good test of GR in the strong field but also reveal new relativistic effects that are observed for the first time. These timing results provide seven PPK parameters, which are more than those from any other known binary pulsars, and some of the parameters need to take higher-order contributions into account. Our following discussion will highlight some novel aspects of the double pulsar from this new set of data.

As mentioned before, the DD model is a compact timing model that uses the solution of the 1 PN two-body problem. However, the precision of timing for the double pulsar is so high that higher-order corrections to the timing model need to be added. For $\dot{\omega}$, 2 PN and the Lense-Thirring effects are needed [54]

$$\dot{\omega} = \dot{\omega}_{1\,\mathrm{PN}} + \dot{\omega}_{2\,\mathrm{PN}} + \dot{\omega}_{\mathrm{LT_A}}\,, \tag{1.24}$$

where $\dot{\omega}_{2\,\mathrm{PN}} = \dot{\omega}_{1\,\mathrm{PN}} f_{\mathrm{O}} V_b^2/c^2$ with

$$f_{\mathrm{O}} = \frac{1}{1-e^2}\left(\frac{3}{2}X_A^2 + \frac{3}{2}X_A + \frac{27}{4}\right) + \left(\frac{5}{6}X_A^2 - \frac{23}{6}X_A - \frac{1}{4}\right), \tag{1.25}$$

where $X_{\mathrm{A}} \equiv m_{\mathrm{A}}/m$. For PSR J0737−3039A, the misalignment angle of $\mathbf{S}_{\mathrm{A}}$ relative to the total angular momentum vector is very small, $\delta_{\mathrm{A}} < 3.2^\circ$ [38]. So Eq. (1.22) is used to calculate $\dot{\omega}_{\mathrm{LT_A}}$. Using values from timing, it was found that $\dot{\omega}_{2\,\mathrm{PN}} \simeq 4.39 \times 10^{-4}\,\mathrm{deg\,yr^{-1}}$ in GR, about 35 times of the measurement error of $\dot{\omega}$ (see Table 1.3). For $\dot{\omega}_{\mathrm{LT_A}}$, except that the moment of inertia of pulsar A (I_{A}) depends on the EOS of NSs, all quantities in Eq. (1.22) are measured with high precision, and we get [60],

$$\dot{\omega}_{\mathrm{LT_A}} \simeq -3.77 \times 10^{-4} \times I_{\mathrm{A}}^{(45)}\,\mathrm{deg\,yr^{-1}}\,, \tag{1.26}$$

where $I_{\mathrm{A}}^{(45)} \equiv I_{\mathrm{A}}/(10^{45}\,\mathrm{g\,cm^2})$. Generally, $I_{\mathrm{A}}^{(45)}$ is of order unit, so $\dot{\omega}_{\mathrm{LT_A}}$ and $\dot{\omega}_{2\,\mathrm{PN}}$ have the same order of magnitude [61].

In Eq. (1.9), the Römer delay depends on the projected semi-major axis x. In Newtonian gravity, the binary mass function describes the relation between the inclination angle i and x by Eq. (1.17). Because of the high precision measurements, the mass function now needs to extend to 1 PN [60],

$$\sin i = \frac{n_{\mathrm{b}} x}{X_{\mathrm{B}}}\frac{c}{V_b}\left[1 + \left(3 - \frac{1}{3}X_{\mathrm{A}}X_{\mathrm{B}}\right)\frac{V_b^2}{c^2}\right], \tag{1.27}$$

with $X_{\mathrm{B}} = m_{\mathrm{B}}/m$. Such an extension was the first time for any binary pulsar system.

GW damping enters the GR equations of motion at 2.5 PN level [c.f. Eq. (1.19)]. For the double pulsar, it is extended to 3.5 PN, with $\dot{P}_b^{3.5\,\mathrm{PN}} = \dot{P}_b^{2.5\,\mathrm{PN}} X^{3.5\,\mathrm{PN}} \simeq -1.75 \times 10^{-17}$; for the factor $X^{3.5\,\mathrm{PN}}$ one can refer to Eqs. (12–13) in Ref. [54]. This value is about 4.5 times smaller than the timing precision of $\dot{P}_b$. The mass loss caused by the spin-down of the pulsars can also contribute to the observed $\dot{P}_b$, and for pulsar A, it is $\dot{P}_{\mathrm{b}}^{\dot{m}_{\mathrm{A}}} = 2.3 \times 10^{-17} \times I_{\mathrm{A}}^{(45)}$. Using constraints from Ref. [33] and the radius-I_A relation in Ref. [65], one gets $\dot{P}_{\mathrm{b}}^{\dot{m}_{\mathrm{A}}} = 2.9(2) \times 10^{-17}$, which is 3 times smaller than the error of $\dot{P}_b^{\mathrm{int}}$. Besides $\dot{P}_b^{\mathrm{int}}$, the non-intrinsic contributions $\dot{P}_{\mathrm{b}}^{\mathrm{Shk}}$ and $\dot{P}_{\mathrm{b}}^{\mathrm{Gal}}$ also need to be considered. These two terms are both functions of the pulsar distance d. The parallax from VLBI and pulsar timing was combined to provide a weighted distance, $d = (735 \pm 60)\,\mathrm{pc}$. Considering all the above, $\dot{P}_b$ is expressed as,

$$\dot{P}_b = \dot{P}_b^{2.5\,\mathrm{PN}} + \dot{P}_b^{3.5\,\mathrm{PN}} + \dot{P}_{\mathrm{b}}^{\dot{m}_{\mathrm{A}}} + \dot{P}_{\mathrm{b}}^{\mathrm{ext}}\,, \tag{1.28}$$

Table 1.3: Orbital parameters of PSR J0737−3039A [60].

Parameter	Value
Projected semi-major axis, $x\,(\mathrm{s})$	1.415028603(92)
Eccentricity, e	0.087777023(61)
Orbital period, $P_b\,(\mathrm{d})$	0.1022515592973(10)
Epoch of periastron, $T_0\,(\mathrm{MJD})$	55700.233017540(13)
Longitude of periastron, $\omega_0\,(\mathrm{deg})$	204.753686(47)
Periastron advance rate, $\dot{\omega}\,(\mathrm{deg\,yr^{-1}})$	16.899323(13)
Einstein delay amplitude, $\gamma\,(\mathrm{ms})$	0.384045(94)
Change rate of orbital period, $\dot{P}_b$	$-1.247920(78)\times10^{-12}$
Logarithmic Shapiro shape, z_s	9.65(15)
Range of Shapiro delay, $r\,(\mu\mathrm{s})$	6.162(21)
NLO factor for signal propagation, q_{NLO}	1.15(13)
Relativistic deformation of orbit, δ_θ	$13(13)\times10^{-6}$
Change rate of projected semi-major axis, $\dot{x}$	$8(7)\times10^{-16}$
Change rate of eccentricity, $\dot{e}\,(\mathrm{s^{-1}})$	$3(6)\times10^{-16}$
Derived parameters	
$\sin i = 1-\exp(-z_s)$	0.999936(+9, −10)
Orbital inclination, $i\,(\mathrm{deg})$	89.35(5) or 90.65(5)
Total mass, $m\,(M_\odot)$	2.587052(+9, −7)
Mass of pulsar A, $m_{\mathrm{A}}\,(M_\odot)$	1.338185(+12, −14)
Mass of pulsar B, $m_{\mathrm{B}}\,(M_\odot)$	1.248868(+13, −11)

where $\dot{P}_{\mathrm{b}}^{\mathrm{ext}} = \dot{P}_{\mathrm{b}}^{\mathrm{Shk}} + \dot{P}_{\mathrm{b}}^{\mathrm{Gal}} = -1.68^{+11}_{-10}\times10^{-16}$, leaving the intrinsic contribution, $\dot{P}_{\mathrm{b}}^{\mathrm{int}} = \dot{P}_b - \dot{P}_{\mathrm{b}}^{\mathrm{ext}} = -1.247752(79)\times10^{-12}$ [60]. The error of $\dot{P}_{\mathrm{b}}^{\mathrm{int}}$ is still dominated by the error of $\dot{P}_b$. In the future improving the timing precision of the observed $\dot{P}_b$ will improve this gravity test.

The Shapiro delay effect in Eq. (1.11) is the leading-order effect caused by the companion's mass influencing the signal propagation. It was obtained by integrating along a straight line and assuming a static mass distribution [12]. For the double pulsar one needs a lensing correction to the Shapiro delay. It restores the fact that pulsar A's radio signal propagates along a curved path. Equation (1.11) is rewritten as $\Delta_{\mathrm{SB}} = -2r\ln\Lambda_u$, and Kramer et al. [60] added a term corresponding to the lensing correction $\delta\Lambda_u^{\mathrm{len}} = 2rc/a_R$, where a_R is the semi-major axis of the relative orbit. Considering a non-static mass distribution, a 1.5 PN correction $\delta\Lambda_u^{\mathrm{ret}}$ from the retardation effect was taken into account. So the signal propagation delay is extended to $\Delta_{\mathrm{SB}} = -2r\ln\left(\Lambda_u + \delta\Lambda_u^{\mathrm{len}} + \delta\Lambda_u^{\mathrm{ret}}\right)$. For the aberration delay Δ_{AB}, considering the rotational deflection delay, Kramer et al. [60] used a lensing correction term, $\mathscr{D}\cos\Phi/\Lambda_u$, where $\Phi = \omega + A_e(u)$. Nevertheless, the next-to-leading-order (NLO) contributions from the Shapiro delay and the aberration delay cannot be tested sepa-

rately in the double pulsar system. These contributions are rescaled with a common factor $q_{\rm NLO}$ to test the significance of NLO signal propagation contributions. The factor $q_{\rm NLO}$ can be fitted in the extended timing model with the double pulsar data.

After providing an extended timing model with higher-order contributions, one can use the timing results in Table 1.3 to determine the masses and test GR. Generally, one needs two PPK parameters to determine the masses of a binary system in GR. However, when including higher-order contributions, the parameters $\dot{\omega}$ and $\dot{P}_b^{\rm int}$ are also functions of I_A, namely $\dot{\omega} = \dot{\omega}(m_A, m_B, I_A)$ and $\dot{P}_b^{\rm int} = \dot{P}_b^{\rm int}(m_A, m_B, I_A)$. Using constraints on the EOS obtained from the binary NS merger event GW170817 [1], one has restriction on I_A. Kramer et al. [60] used the information of I_A and the timing values of $\dot{\omega}$ and s and got the masses of the binary,

$$m_{\rm A} = 1.338185(+12, -14)\, M_\odot\,, \tag{1.29}$$

$$m_{\rm B} = 1.248868(+13, -11)\, M_\odot\,, \tag{1.30}$$

$$m = 2.587052(+9, -7)\, M_\odot\,. \tag{1.31}$$

If one ignores any existing constraints on the EOS of NSs and simultaneously determine m_A, m_B and I_A, one needs three PPK parameters. With $\dot{\omega}(m_A, m_B, I_A)$, $\dot{P}_b^{\rm int}(m_A, m_B, I_A)$ and $s(m_A, m_B)$, one not only gets the masses of the system, but also constrains I_A to $I_A < 3.0 \times 10^{45}\,{\rm g\,cm^2}$ with 90% confidence, complementing the constraints from LIGO/Virgo [1, 64] and NICER [103] observations.

The double pulsar provides seven PPK parameters, $\{\dot{\omega}, \gamma, \dot{P}_b, r, s, \Omega_B, \delta_\theta\}$, and a theory-independent parameter R (c.f. Table 1.3). For δ_θ, its measured value is not significant, so it is not used in testing GR. When a value for I_A is chosen, these PPK parameters are functions of binary masses and those well-measured Keplerian parameters. So using six measured PPK parameters and the mass ratio R, one can perform five independent tests of GR, as shown in Fig. 1.4 [58].

As mentioned earlier, including the 3.5 PN contribution from GW damping and removing the mass loss and non-intrinsic contributions, one has [60],

$$\dot{P}_{\rm b}^{\rm GW} = \dot{P}_{\rm b}^{\rm int} - \dot{P}_{\rm b}^{\dot{m}_{\rm A}} = -1.247782(79) \times 10^{-12}\,. \tag{1.32}$$

Using the masses shown in Eqs. (1.29–1.30), the predicted value from GR is,

$$\dot{P}_{\rm b}^{\rm GW,GR} = \dot{P}_{\rm b}^{\rm GW,GR(2.5\,PN)} + \dot{P}_{\rm b}^{\rm GW,GR(3.5\,PN)} = -1.247827(+6, -7) \times 10^{-12}\,.$$

This value provides the most precise test for the GW quadrupolar emission [60], $\dot{P}_b^{\rm GW}/\dot{P}_b^{\rm GW,GR} = 0.999963(63)$. It is also the most precise result among the different independent tests that one can obtain from this system. It is in agreement with GR at a level of 1.3×10^{-4} with 95% confidence [60]. Other independent tests are listed in Table 1.4. PSR J0737−3039A/B provides the strictest limit on GR than any other binary pulsar systems.

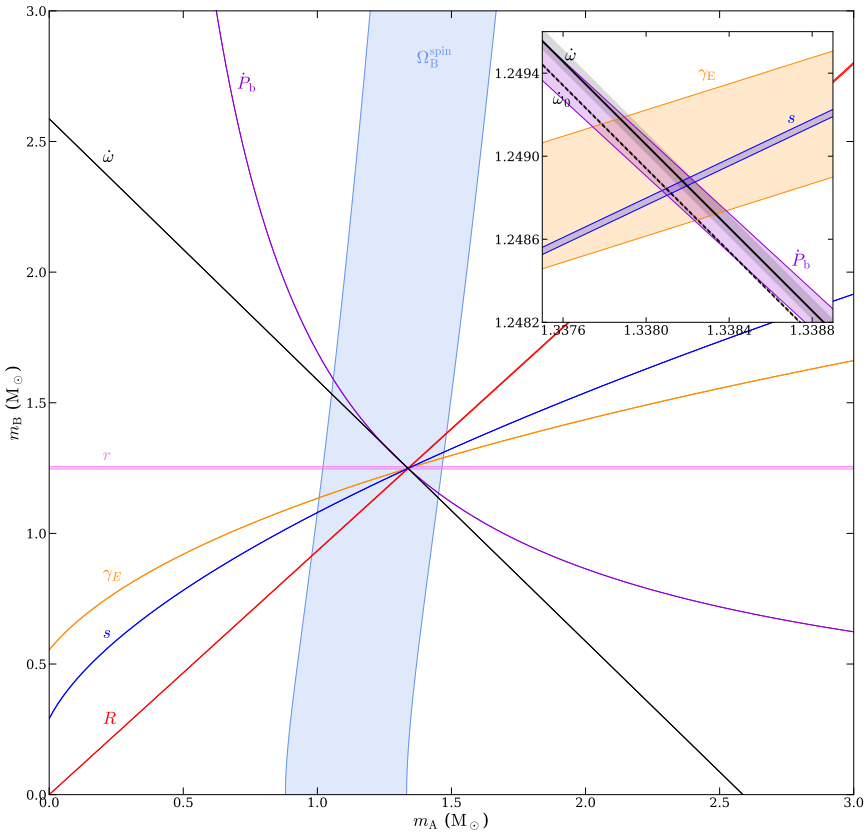

Fig. 1.4: Mass-mass diagram of PSR J0737−3039 [60]. It shows the constraints from six PPK parameters and the mass ratio R. The inset shows the zoom-in region of the intersection of these measurements. The solid black line for $\dot{\omega}$ responds to $I_A^{(45)} = 1.32$. The gray band indicates the range for $\dot{\omega}$ with a changing $I_A^{(45)}$. The dashed black line for $\dot{\omega}_0$ does not contain the contribution of the Lense-Thirring effect.

1.3.3 The triple system: PSR J0337+1715

Binary pulsar systems provide us with great opportunities to test GR. There are also some pulsars that exist in more complicated systems. For example, PSR B1257+12, a pulsar moves in a system that contains at least three low-mass planets. This pulsar helped people discover the first exoplanet system [121, 77]. Here we focus on PSR J0337+1715, which is a 2.7-ms pulsar in a hierarchical triple system with two white dwarf (WD) companions [87]. The inner pulsar-WD system is a 1.6-d circular orbit system and the mass of the WD is $0.19751(15)\,M_\odot$. The outer orbit is wider,

Table 1.4: Relativistic effects measured in the double pulsar system and the resulting independent strong-field tests of GR [60]. The right column shows the ratio between the observed quantity and its prediction in GR.

Parameter	Ratio
Shapiro delay shape, s	1.00009(18)
Shapiro delay range, r	1.0016(34)
Time dilation, γ	1.00012(25)
Periastron advance, $\dot{\omega}$	1.000015(26)
Change rate of orbital period, $\dot{P}_b$	0.999963(63)
Orbital deformation, δ_θ	1.3(13)
Spin precession, $\Omega_{\rm B}$	0.94(13)
Tests of higher-order contributions	
Lense-Thirring contribution to $\dot{\omega}$, $\lambda_{\rm LT}$	0.7(9)
NLO signal propagation, $q_{\rm NLO}$ [total]	1.15(13)

with $P_b = 327.2\,\mathrm{d}$, and the WD's mass is $0.4101(3)\,M_\odot$ [87]. The special system composition and high-precision timing results of PSR J0337+1715 make it an ideal laboratory that can provide a strong equivalence principle (EP) test of GR [5, 111].

The principle of equivalence has played an important role in the development of theories of gravity. In Newton's gravity, the principle of equivalence is the cornerstone of the theory. It assumes that the inertial mass equals the passive gravitational mass. Now, this is so-called the weak EP (WEP), and its alternative statement is that the trajectory of a freely falling test body is independent of the body's internal structure and composition. With the development of gravity theory, the principle of equivalence has been extended. Except for satisfying the WEP, one believes that a gravity theory should also satisfy the local Lorentz invariance (LLI) and local position invariance (LPI). Combined with WEP, we call it the Einstein EP (EEP). In the EEP, LLI states that a non-gravitational experiment does not depend on the velocity of the freely falling reference frame, and LPI states that the outcome of any local non-gravitational experiment is independent of when and where the experiment is performed. Metric theories of gravity satisfy the EEP [118]. The strictest bound comes from the strong EP (SEP), it demands that WEP is valid for self-gravitating bodies as well, and a gravitational experiment needs to embody LLI and LPI simultaneously. For now, GR seems to be the only viable metric theory that satisfies SEP completely. So testing SEP is equal to testing GR in this sense.

There are many methods to test SEP, and one of them is considering the universality of free fall of two self-gravitating bodies in an external gravitational field. Some tests from the Solar System have been done and provided tight constraints on the violation of the SEP, but the bodies in the Solar System are weak in terms of self-gravity. For instance, the fractional binding energy difference between the

Earth and the Moon is $\sim -4\times10^{-10}$. Pulsar-WD systems can provide an evident fractional binding energy difference between the NS and the WD, at the order of -0.1, which is many orders of magnitude larger than the Earth-Moon system's difference. If the acceleration difference between the pulsar and the WD is present, it will lead to a characteristic change in its orbital eccentricity evolution. However, a pulsar-WD system's free fall in the Galactic gravitational field cannot provide a tight limit on the SEP violation parameter Δ, because the Galactic gravitational acceleration at the location of the pulsar is comparably weak, $\sim 2\times10^{-8}\,\mathrm{cm\,s^{-2}}$. For example, PSR J1713+0747 provides a constraint, $\Delta < 0.002$ [133]. For the triple system PSR J0337+1715, the outer WD can provide an external gravitational acceleration for the inner PSR-WD system, and its strength is $\sim 0.17\,\mathrm{cm\,s^{-2}}$, which is $\sim 10^7$ times larger than the Galactic gravitational acceleration. So PSR J0337+1715 makes a significant improvement on the constraint of the SEP violation parameter, $\Delta < 2.6\times10^{-6}$ [5] and $\Delta = (0.5\pm0.9)\times10^{-6}$ [111] by two independent groups.

1.4 Neutron Star Structures

As introduced in the previous section, pulsars, which are rotating NSs, can provide unique possibilities to probe the strong-field region of GR. With a typical mass of $1.4\,\mathrm{M}_\odot$ and a radius of 12 km, NSs not only provide the strong-field environment of gravity, but also are the most extreme laboratory of particle physics. In this section, we will introduce the basic theory describing the NS structures, and show some properties of a single NS that can be measured with pulsar timing technique and other observations. Differing from the tests of gravity from binary pulsar systems, which use the dynamic aspect of the gravity theory, testing gravity with a single NS provides the properties of an equilibrium state. In the following, we take $G = c = 1$ except when the units are written out explicitly, and the convention of the metric is $(-,+,+,+)$.

The basic information of a compact star is its mass and radius, which reveal the inner structure and interaction among the star's components. In GR, to derive the structure of a spherical, non-rotating NS, we begin with the Einstein's field equations, $G_{\mu\nu} = 8\pi T_{\mu\nu}$, together with some specific matter model, for example a perfect fluid, $T^{\mu\nu} = (\rho + p)u^\mu u^\nu + p g^{\mu\nu}$. Then one adopts the metric of a static, spherically symmetric spacetime

$$\mathrm{d}s^2 = -\left(1 - \frac{2m(r)}{r}\right)\mathrm{d}t^2 + \frac{\mathrm{d}r^2}{1-2m/r} + r^2\mathrm{d}\Omega^2\,, \tag{1.33}$$

and inserts it into the field equations. The equation of a star is described by the Tolman-Oppenheimer-Volkov (TOV) equation [84, 110]

$$\frac{\mathrm{d}p}{\mathrm{d}r} = -\frac{(\rho+p)(m+4\pi r^3 p)}{r(r-2m)}\,, \tag{1.34}$$

where $m(r)$ is called the mass inside the sphere of radius r, defined by the integral, $m(r) = \int_0^r 4\pi r^2 \rho \mathrm{d}r$, just as in the Newtonian theory. Results show that for any physical realizable matter, $m(r)/r \leq 0.485$, so that the right hand side of Eq. (1.34) is never singular [13]. The dimensionless ratio between a star's mass and radius, $C \equiv M/R$, is called the compactness of the star, which represents how compact a star is. For Schwarzschild black holes (BHs) in GR this number is equal to 0.5 and for a typical NS, the compactness can reach 0.2. As a comparison, the compactness of the Sun is only 2×10^{-6}. This is crucial for the SEP in Sec. 1.3.3.

To complete the above equations, a relation called the EOS between the pressure p and the energy density ρ is needed. For a simple fluid in local thermodynamic equilibrium, there always exists a relation of the form, $p = p(\rho, S)$, where S is the specific entropy. For old NSs that are sufficiently cold or under the assumption of constant entropy, we can restrict this relation to a one-parameter functional, $p = p(\rho)$.

For a given EOS, one can then solve the TOV equation with initial condition $\rho|_{r=0} = \rho_0$ to get the structure of a NS. With the uniqueness theorems for ordinary differential equations, the solutions will form a one-parameter sequence with the parameter being the central density. Correspondingly, for a given theory of gravity, this sequence, the so-called mass-radius relation, also uniquely determines the underlying EOS [68]. The total mass of the NS is $m(R)$, where R is the radius of the surface defined by $p(R) = 0$. For a normal NS that is gravitationally self-bounded, the density also approaches zero at the star's surface, i.e. $\rho(R) = 0$. But if a NS consists of quarks or strangeons that are not gravitationally self-bounded, there can be a density discontinuity at the surface of the star [28, 89, 43].

In Fig. 1.5 we show some EOSs and the corresponding M-R relations for NSs. The EOSs inside the NSs are still not clear today. The main components of NSs are mainly regarded as neutrons, but there also should be protons, electrons, muons, and so on. It remains an unsolved problem in quantum chromodynamics for calculating the super-dense nuclear matter at low temperatures. Furthermore, there are some arguments that the ingredients of NSs should be quarks or strangeons [120, 122, 63, 43]. From Fig. 1.5, we can see that there is large difference between different EOS models, especially between the models for a normal NS and models for a quark or a strangeon star. For those NSs that are not gravitationally self-bounded, the behavior at the low mass limit is like a star with constant density. This feature still holds approximately when the mass of the star increases, and leads to various differences in other aspects like the moment of inertia and the star oscillation frequency (see e.g. Ref. [67]). But one can notice that all of these EOS models have a maximum mass in their M-R relations. For WDs this maximum mass is famously known as the Chandrasekhar limit, which is around $1.4\,\mathrm{M}_\odot$. Due to the uncertainty in the EOS, the maximum mass of NSs can vary largely, from about $1.5\,\mathrm{M}_\odot$ to over $3\,\mathrm{M}_\odot$. Known as the turning point theory [47], a NS with mass and radius crossed the maximum mass point in the M-R relation becomes unstable. So the discover of supermassive NSs can help us constrain the EOS of NSs. The two horizontal lines in Fig. 1.5b are the observed masses of PSR J0348+0432 [4] and PSR J1614−2203 [39], and then EOSs which cannot support a maximum mass higher than $2\,\mathrm{M}_\odot$ are excluded by

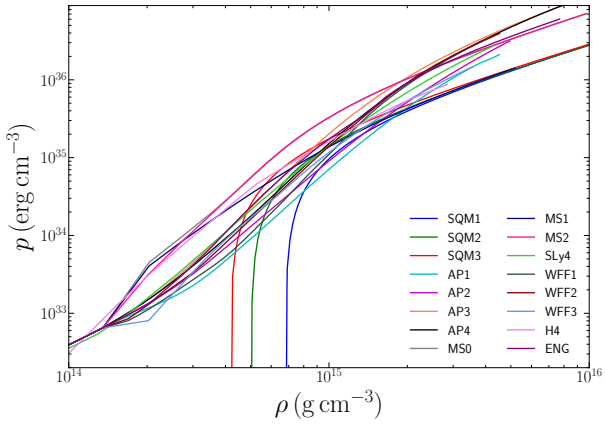

(a) EOSs

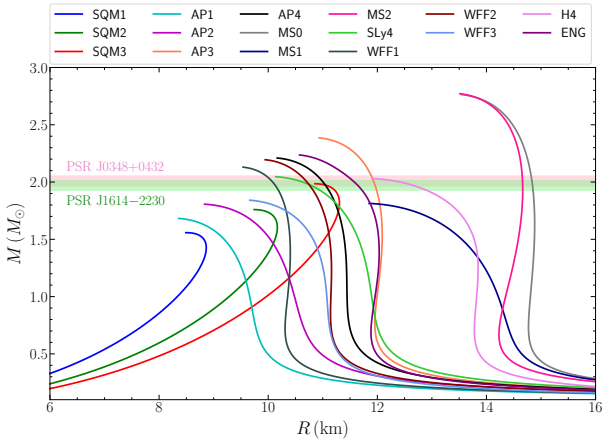

(b) *M*-*R* relations

Fig. 1.5: EOSs for NSs [66] and the related *M*-*R* relations (figure courtesy of Y. Gao). The horizontal lines in Fig. 1.5b are the observed masses for two massive pulsars [4, 39]. The SQM model is related to quark stars [66]. Curves passing the highest point in their *M*-*R* relations are cut off, as they represent unstable NSs.

these observations. But if one considers gravity theories different from GR, the *M*-*R* relation of the same EOS can vary largely from their GR counterpart. Thus a precise measurement of the *M*-*R* relation can constrain not only the EOS but also the gravity theory [102]. Previous measurements from the NICER satellite by modeling the thermal x-ray waveform of the isolate pulsar PSR J0030+0451 give a constraint on the mass and equatorial radius of the star simultaneously [90, 81]. But measurements from more NSs with higher precision are still needed.

The above discussion is based on the assumption of a static star. For real pulsars, they can have spin periods from several milliseconds to tens of seconds (see Fig. 1.1). Some studies have shown that fast-rotating NSs can support a larger maximum mass and it will have important influence on the evolution of the binary NS merger remnant [9, 132]. One can estimate the maximum angular velocity of a NS from the Newtonian theory, $\Omega_{\rm max} = (M/R^3)^{1/2}$, which is related to the mass shedding limit. For a typical NS, this corresponds to a spin period of about 0.5 ms. Thus for most pulsars, the approximation of slow rotation is sufficient, and in this case, the mass-radius relation of NSs will not change, to the first order in Ω.

The basic property related to rotation is the moment of inertia. In GR, the moment of inertia of a slowly rotating NS can be calculated through the slow rotation approximation [49]. Under this approximation the metric is writen as

$$\begin{aligned} {\rm d}s^2 = g_{\mu\nu}{\rm d}x^\mu {\rm d}x^\nu = &-\left(1-\frac{2m}{r}\right){\rm d}t^2 + \frac{{\rm d}r^2}{1-2m/r} + r^2\left({\rm d}\theta^2 + \sin^2\theta {\rm d}\phi^2\right) \\ &+ r^2\sin^2\theta\left({\rm d}\phi + (\omega(r)-\Omega)\,{\rm d}t\right)^2 , \end{aligned} \tag{1.35}$$

where $m(r)$ is just the same as that solved from the TOV equation for a non-rotating NS, Ω is the angular velocity of the star and $\omega(r)$ shows the effect of frame dragging. An observer falling freely from infinity to r will have an angular velocity $\Omega - \omega(r)$ to the first order in Ω, thus seeing the fluid element at r has an angular velocity $\omega(r)$. Function $\omega(r)$ is determined by the linear differential equation,

$$\frac{{\rm d}^2\omega}{{\rm d}r^2} = \frac{4\pi r}{r-2m}(\rho+p)\left(r\frac{{\rm d}\omega}{{\rm d}r}+4\omega\right) - \frac{4}{r}\frac{{\rm d}\omega}{{\rm d}r} . \tag{1.36}$$

The boundary condition is $\omega = \Omega$ when r goes to infinity. Besides that, in order to keep ${\rm d}^2\omega/{\rm d}r^2$ to be finite at the origin, we have ${\rm d}\omega/{\rm d}r|_{r=0} = 0$. The angular momentum J carried by the star can be read out from the asymptotic behavior of $g_{t\phi}$ at $r\to\infty$, $g_{t\phi} = (\omega-\Omega)r^2\sin^2\theta \to -2J\sin^2\theta/r$, which indicates that

$$J = \frac{1}{6}\frac{{\rm d}\omega}{{\rm d}r}r^4\Big|_{r\to\infty} . \tag{1.37}$$

The moment of inertia of the star thus is defined to be

$$I = \frac{J}{\Omega} = \frac{r^4}{6\omega}\frac{{\rm d}\omega}{{\rm d}r}\Big|_{r\to\infty} . \tag{1.38}$$

Combining with Eq. (1.36), the moment of inertia of the star can be calculated from

$$\frac{{\rm d}I(r)}{{\rm d}r} = \frac{2}{3}\frac{4\pi r^4(\rho+p)}{1-2m/r}\left(1-\frac{5}{2}\frac{I}{r^3}+\frac{I^2}{r^6}\right) , \tag{1.39}$$

with initial condition $I(r=0)=0$. This equation, similar to the TOV equation, can be regarded as the corresponding equation in the Newtonian theory with some correction terms that come from GR.

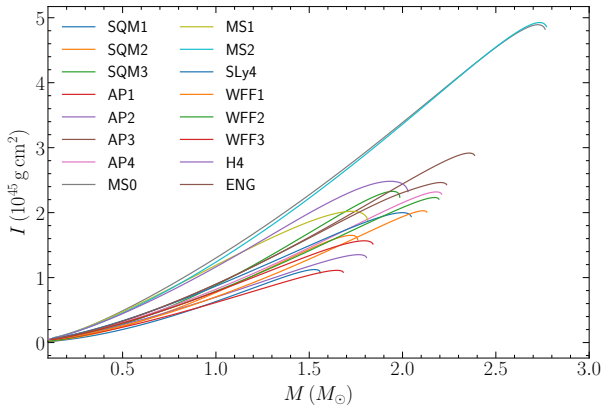

Fig. 1.6: Moment of inertia of NSs with different EOSs (figure courtesy of Y. Gao). Unstable solutions are cut off as in Fig. 1.5b.

In Fig. 1.6 we show the NS moment of inertia with some EOSs. It is relatively hard to measure the NS moment of inertia directly, because there is no leading order effect caused by the current in Newtonian gravity. Some indirect measurements come from modeling the X-ray profile of X-ray pulsars and combining with proper universal relations [103]. Notably, as explained in Sec. 1.3.2, the observations of the double pulsar binary starts to constrain the moment of inertia through the spin-orbit coupling [60]. Measuring the moment of inertia independently is valuable in gravity tests as it relates to the universal relationship that will be discussed later.

There are some other quantities that describe the NS structure and can be measured today. One example that will be used later is the tidal Love number of NSs [51]. This quantity describes how easily an object can be tidally deformed and it can be measured from the GW signal of colliding NSs [1]. At the early stage of the inspiral, the motion of the binary system is dominated by the point-mass dynamics, which is similar to, but with higher-order corrections, what we discussed in Sec. 1.2. Near the end of the inspiral, the non-uniform gravity field of the companion will cause both stars to be tidally deformed, and the internal degrees of freedom of the stars begin to influence the GW signal. The observation of the famous event GW170817 set an upper limit on the NS tidal Love number that $\tilde{\Lambda} \lesssim 800$, which excludes some EOSs that are too stiff [1].

There is a problem that comes up when we want to test strong-field gravity with NS structures: the uncertainties in the EOS [96, 102]. Nuclear physics in the laboratory cannot tell us which EOS is correct yet. Thus, for example, the mass-radius relation of NSs depends not only on the theories of gravity but also on the choice of EOSs. If a measurement tells us the mass and radius of a NS, we can equally conclude that in GR, some EOSs are consistent with this measurement, or for a specific EOS, some gravity theories can pass the test. Thus, in order to constrain gravity

theories, one needs to consider various reasonable EOSs, or one has to break the degeneracy between gravity theories and nuclear physics.

One way to break such a degeneracy is to find relations that are not sensitive to the EOS but still depend on the gravity theory. In GR, such relations do exist. One famous example of such relations is the "I-Love-Q" relation between the dimensionless moment of inertia, the tidal Love number and the quadrupole moment of NSs (see, e.g. Fig. 1 in Ref. [125]). The deviations from the common relation caused by variations in EOS can be smaller than 1%. As the tidal Love number can be measured by GWs from colliding NSs as mentioned before, measuring the moment of inertia of NSs thus becomes very important.

Many efforts have been done to understand why there are such universal relations existing in GR and many other gravity theories [126]. The possible physical picture is some approximate symmetries emergent when the stars become more and more compact and they are responsible for the universality [126]. For example, the isodensity self-similarity leads to a constant eccentricity profile which will minimize the energy of the system [62]. There are also some mathematical approaches showing that the "I-Love" relation is perturbatively insensitive with respect to changes in the polytropic index of the EOS around the incompressible limit [18].

There are many other universal relations known today, for example the relation between the Love number and the f-mode frequency, the no-hair-like relations, the *I-C* relation and so on [126, 44]. Testing strong-field gravity with universal relations seems promising, though there are still some subtle issues that need to be studied further [102]. In principle, to test gravity with universal relations, one needs to measure several quantities independently for the same NS, for example, the Love number and the moment of inertial. But usually, different quantities are proper to measure in different systems, which correspond to different NSs with different masses. One way to go through this problem is to measure those quantities for many different NSs with similar masses [102], for example around $1.4\,\mathrm{M}_{\odot}$. Then one can combine these results to a universal relation by doing an interpolation on the mass. Another possible method is to establish universal relations that relate quantities in different masses [92].

1.5 Tests of Alternative Gravity Theories

Though Einstein's GR has passed all present tests with flying colors, there is still great enthusiasm for modified gravity theories [118, 10, 117, 100]. Those alternative gravity theories may arise as low-energy effective theories of some quantum field theories or motivate from dark matter and dark energy problems. As they provide the explicit form of how can a theory deviate from GR, studying these modified gravity theories is also important and intuitive in testing gravity. In the following, we will describe some basic aspects of modified gravity theories by illustrating two concrete examples: scalar-tensor gravity and massive gravity.

1.5.1 Scalar-tensor theory

Scalar-tensor gravity theories are the simplest and mathematically well-posed extension to GR by including some scalar fields that are non-minimally coupled in the Lagarangian of gravity. A general class of scalar-tensor gravity theories with one extra scalar field Φ have the following action in the physical frame (or the so-called Jordan frame) [25]

$$S = \frac{c^4}{16\pi G_*}\int \frac{\mathrm{d}^4x}{c}\sqrt{-\tilde{g}}[F(\Phi)\tilde{R} - Z(\Phi)\tilde{g}^{\mu\nu}\partial_\mu\Phi\partial_\nu\Phi - U(\Phi)] + S_m[\psi_m;\tilde{g}_{\mu\nu}]\,, \tag{1.40}$$

where G_* denotes a bare gravitational coupling constant and $S_m[\psi_m;\tilde{g}_{\mu\nu}]$ is the action of standard matters; $\tilde{R}$ and $\tilde{g}$ are the Ricci scalar and the metric determinant calculated from the "physical metric" $\tilde{g}_{\mu\nu}$, respectively. In this kind of theories the WEP is satisfied because all the matter variables ψ_m are coupled to the same metric $\tilde{g}_{\mu\nu}$. It is often convenient to rewrite this action in a canonical form by redefining Φ and $\tilde{g}_{\mu\nu}$ via [22]

$$g^*_{\mu\nu} = F(\Phi)\tilde{g}_{\mu\nu}\,, \tag{1.41}$$

$$\varphi = \pm\int \mathrm{d}\Phi\left[\frac{3}{4}\frac{F'^2(\Phi)}{F^2(\Phi)} + \frac{1}{2}\frac{Z(\Phi)}{F(\Phi)}\right]^{1/2}. \tag{1.42}$$

It leads to an action in the Einstein frame

$$S = \frac{c^4}{16\pi G_*}\int \frac{\mathrm{d}^4x}{c}\sqrt{-g_*}[R_* - 2g_*^{\mu\nu}\partial_\mu\varphi\partial_\nu\varphi - V(\varphi)] + S_m[\psi_m;A^2(\varphi)g^*_{\mu\nu}]\,. \tag{1.43}$$

Now R_* and g_* are calculated from the new metric $g^*_{\mu\nu}$, and the potential term

$$V(\varphi) = F^{-2}(\Phi)U(\Phi)\,. \tag{1.44}$$

In this form the matter fields are coupled to the conformal metric $A^2(\varphi)g^*_{\mu\nu}$ instead of $g^*_{\mu\nu}$ itself, where the conformal coupling function

$$A(\varphi) = F^{-1/2}(\Phi)\,. \tag{1.45}$$

As the matter fields couple directly to the metric $\tilde{g}_{\mu\nu}$, this metric is the one that can be measured by laboratory clocks and rods and it is called the physical metric. While the canonical representation is often more convenient for calculation as it decouples the spin-0 excitation of φ and the spin-2 excitation of $g^*_{\mu\nu}$.

For different choices of the coupling function $A(\varphi)$ and the potential $V(\varphi)$, one gets different classes of scalar-tensor theories. Note that one can always work in

some appropriate units that the asymptotic value of $A(\varphi) = 1$, which means in these units, the Einstein metric and the physical metric asymptotically coincide.

The field equation can be derived from Eq. (1.43) by taking variations with respect to $g^*_{\mu\nu}$ and φ [123]

$$R^*_{\mu\nu} = 2\partial_\mu\varphi\partial_\nu\varphi + 8\pi G_* \left(T^*_{\mu\nu} - \frac{1}{2}T^* g*_{\mu\nu}\right) + \frac{1}{2}g^*_{\mu\nu}V(\varphi)\,, \tag{1.46}$$

$$\Box\varphi = -4\pi G_*\alpha(\varphi)T_* + \frac{1}{4}\frac{\mathrm{d}V(\varphi)}{\mathrm{d}\varphi}\,, \tag{1.47}$$

where $T^{\mu\nu}_* = 2(-g_*)^{-1/2}\delta S_m/\delta g^*_{\mu\nu}$ and $\alpha(\varphi) = \partial \ln A(\varphi)/\partial\varphi$. The quantity $\alpha(\varphi)$ plays the role of the coupling strength between the scalar field and ordinary matter, and in general, it can be field-dependent.

Since any function $a(\varphi) \equiv \ln A(\varphi)$ can be expanded when the scalar field is weak as

$$a(\varphi) = \alpha_0(\varphi - \varphi_0) + \frac{1}{2}\beta_0(\varphi - \varphi_0)^2 + \cdots\,, \tag{1.48}$$

it has been shown that, for $V(\varphi) = 0$, in the appropriate units that $a(\varphi_0) = 0$, all measurable quantities depend only on the first two coefficients α_0 and β_0 of the expansion at the 1 PN level for weakly self-gravitating objects [25]. In the PPN formalism [118], only two parameters $\gamma^{\rm PPN}$ and $\beta^{\rm PPN}$ deviate from GR (in which $\gamma^{\rm PPN} = \beta^{\rm PPN} = 1$), and they are given by

$$\gamma^{\rm PPN} = 1 - \frac{2\alpha_0^2}{1+\alpha_0^2}\,, \qquad \beta^{\rm PPN} = 1 + \frac{\alpha_0^2\beta_0}{2(1+\alpha_0^2)^2}\,. \tag{1.49}$$

One can also find that the effective gravitational constant between two bodies is $G = G_*(1+\alpha_0^2)$ in the weak field.

A famous theory, which also may be regarded as the simplest case for scalar-tensor gravity, is the Brans-Dicke theory [14], where there is a varying gravitational constant. In the scalar-tensor formalism, the Brans-Dicke theory is equivalent to

$$a(\varphi) = \alpha_0\varphi + \text{const.}\,, \qquad V(\varphi) = 0\,, \tag{1.50}$$

and in this theory there is a field-independent coupling strength, $\alpha(\varphi) = \alpha_0$. Solar system experiments including light deflection, time delay and frequency shift measurements made with the Cassini spacecraft have set limit on the coupling strength of the scalar field that $\alpha_0^2 \lesssim 1\times10^{-5}$ [88, 91, 11], which tightly constrains the deviations from GR in the weak-field region.

Things can be much different for systems including strongly self-gravitating objects like NSs. It was found that a wide class of scalar-tensor theories can exhibit nonperturbative behaviors called spontaneous scalarization for strong-field objects [26, 34]. As those theories can pass all the weak-field gravity tests while pro-

viding large deviations from GR in the strong-field region and still keep good mathematical behaviors, they largely enhance the interests in studying such theories.

For strongly self-gravitating objects, one can define the effective scalar charge of an object A by $\alpha_A = \partial \ln m_A / \partial \varphi_0$, or equivalently by the asymptotic behavior of the scalar field [25] $\varphi = \varphi_0 - G_* m_A \alpha_A / r + O\left(1/r^2\right)$. The Newtonian gravitational coupling between two bodies A and B can be described by the effective coupling constant, $G_{AB} = G_*(1 + \alpha_A \alpha_B)$.

A simple theory that can have spontaneous scalarization is called the Damour-Esposito-Farèse (DEF) theory, which is widely studied [26, 22]. It can be described by $A(\varphi) = e^{\beta\varphi^2/2}$ and $V(\varphi) = 0$, and the asymptotic value φ_0 of φ here we set to be zero. With arbitrary choice of the asymptotic value φ_0, the DEF theory is just a simple choice with $\alpha_0 = \beta\varphi_0$, $\beta_0 = \beta$ in Eq. (1.48). In this theory, the coupling strength $\alpha(\varphi) = \beta\varphi$ is a linear function of φ.

The name spontaneous scalarization used by Damour and Esposito-Farèse comes from the analogy to the phenomenon of spontaneous magnetization of a ferromagnet [27, 94]. In the DEF theory, the trivial case that $\varphi = 0$ is always a solution to the field equations. In fact this solution is identical with that in GR. In the weak-field region, as we have set $\varphi_0 = 0$, the DEF theory reduces to GR so it can pass any weak-field gravity tests that GR can pass. But for a strongly self-gravitating body, a large scalar charge may be produced spontaneously, like a ferromagnet will have spontaneous magnetization at low temperature. The solution with a non-vanish scalar charge is energetically favored when the star's baryon mass exceeds the critical mass [26, 34].

One can also understand this phenomenon by analyzing the instability of the perturbation in the scalar field [86]. To the linear order in φ, the field equations become

$$R^*_{\mu\nu} = 8\pi\left(\tilde{T}_{\mu\nu} - \frac{1}{2} g^*_{\mu\nu}\tilde{T}\right), \tag{1.51}$$

$$\Box\varphi = -4\pi\tilde{T}\beta\varphi\,. \tag{1.52}$$

For matter described by a perfect fluid, we have $\tilde{T} = \tilde{\rho} + 3\tilde{p}$, which is negative for ordinary matter. Thus the right-hand side of Eq. (1.54) is negative for a negative β, and the scalar field can suffer the tachyonic instability for a sufficiently negative β. Interestingly, it has been shown in some works that for highly compact NSs with certain EOSs, $\tilde{T}$ can be positive, which leads to a spontaneous scalarization for $\beta > 0$ [80].

For those scalar-tensor theories with spontaneous scalarization, the weak-field tests cannot constrain their parameter space efficiently, but they still can be constrained from strong-field tests. In scalar-tensor theories, the energy loss of a system can be carried by both the spin-2 GWs and spin-0 scalar waves to infinity. For those theories with spontaneous scalarization, NSs can carry a large number of scalar charges, which will cause a much enhanced gravitational dipolar radiation for a scalarized NS in a binary. To the leading order, it will contribute an additional decay rate of the binary orbital period via [27]

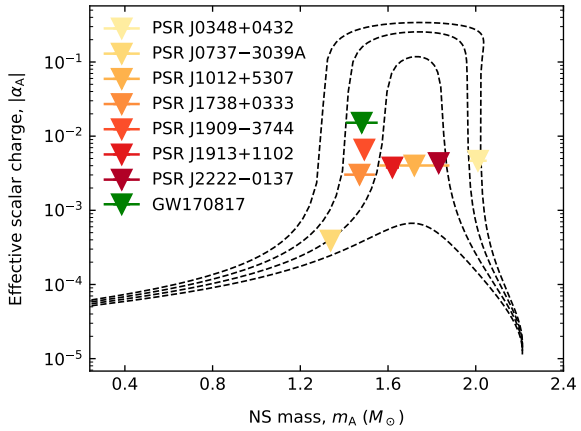

Fig. 1.7: The dashed black curves show the effective scalar charge in the DEF theory with $|\alpha_0| = 10^{-5}$ and $\beta_0 = -4.8, -4.6, -4.4, -4.2$ from top to bottom repectively. The EOS is assumed to be AP4. The observational bounds from different binary pulsars and a GW event are denoted by the triangles [97].

$$\dot{P}_b^{\rm dipole} = -\frac{2\pi G_*}{c^3}(1+e^2/2)(1-e^2)^{-5/2}\frac{2\pi}{P_b}\frac{m_A m_B}{M}(\alpha_A-\alpha_B)^2\,. \qquad (1.53)$$

For some binary pulsars, while a NS has a significant scalar charge, its companion, for example a WD, can only take a vanishingly small scalar charge $\alpha_B \to 0$ as it is a weak-field object. Therefore, NS-WD binaries can be the most sensitive probe to constrain the parameter space of spontaneous scalarization [42]. There is also study showing that for NS-NS binaries with significant difference in the masses of the components can also be excellent laboratories [130]. Besides that, it has been proven that the no-hair theorem still holds in many scalar-tensor theories, which means that the BHs in those theories cannot carry a scalar charge. So that although the binary BHs in those theories will not excite dipole radiation, the NS-BH binaries can still provide abundant information about the underlying gravity theory [69, 98].

Figure 1.7 illustrates the constraints on the effective scalar charges from the gravitational dipole radiation of seven binary pulsar systems and one GW event [97, 130]. Note that in this figure, a specific EOS, AP4, is used to draw the curves. In principle, the uncertainty in the NS EOS will entangle with the gravity test. Nevertheless, with enough well-measured binary pulsar systems, one can set a limit on the whole mass range for NSs, and studies have shown that for each reasonable EOS, the parameter space for spontaneous scalarization in the DEF theory is now very small. In Refs. [99, 131, 46, 130], by using the Bayesian parameter estimation, the possibility of the spontaneous scalarization for an effective coupling larger than 10^{-2} for DEF theory is basically closed, no matter what the underlying EOS of NS is.

As the parameter space for spontaneous scalarization in the initial DEF theory is largely constrained by pulsar timing observation, a natural way to avoid the constraints while keeping the phenomenon of spontaneous scalarization is to consider massive scalar-tensor theories [86, 34]. For example one can consider the DEF theory but with $V(\varphi) = 2m^2\varphi^2$, where m is the mass of the scalar field. The linearized field equation of the scalar field now becomes

$$\Box\varphi = (m^2 - 4\pi\tilde{T}\beta)\varphi\,. \tag{1.54}$$

It shows that the mass term of the scalar field will suppress the existence of spontaneous scalarization [86]. Nevertheless, the spontaneous scalarization can still happen for massive scalar-tensor theories. But with a mass term, the asymptotic value of the scalar field is suppressed exponentially in a Yukawa fashion, which means by definition the scalar charge of a scalarized NS vanishes. Thus no significant dipole radiation will go to infinity. What is more, when the Compton wavelength of the scalar field is smaller than the orbital separation of the binary, the modification with respect to GR in the orbital dynamics will also be suppressed exponentially, which causes the pulsar timing observation hardly setting strong constraints in some parameter space of massive scalar-tensor theories. Fortunately, this kind of theory can still be constrained via the tidal deformability measurement from GWs (see e.g. Refs. [123, 55]). This is true for the reason that a scalarized NS can have large difference in radius compared to that in GR, while the tidal deformability is very sensitive to the star's radius. In this sense, combining pulsar timing observation and GW observation can probe a large parameter space of scalar-tensor theories [99].

In recent years, some variants of scalar-tensor theories triggered great enthusiasm as they can provide solutions for scalarized BHs, in contrast to the no-hair theorem (see Ref. [34] for a review). One example of those theories is the scalar-Gauss-Bonnet theory, which includes a topological Gauss-Bonnet term,

$$\mathscr{G} = R_{\alpha\beta\gamma\delta}R^{\alpha\beta\gamma\delta} - 4R_{\alpha\beta}R^{\alpha\beta} + R^2\,, \tag{1.55}$$

which is coupled to the scalar field [35, 104, 124]. Scalarization of NSs in such kinds of theories can be very different from those in the DEF theories. It also provides a new field where observations of compact objects, including NSs and BHs, are crucial to revealing the strong-field information of gravity. More examples of other variants of scalar-tensor theories that pass current binary-pulsar tests can be found in Ref. [34].

As already discussed, the theories of gravity can sometimes degenerate with the EOS of NSs. One way to break the degeneracy is to find those universal relations that do not depend on the EOS. We have shown that such universal relations do exist in GR, and in fact, this can still be true for some modified gravity. For some theories without spontaneous scalarization, universal relations in GR, like the I-Love-Q relation, are still valid. That means in modified theories, these relations also only weakly depend on the EOS of NSs [126], but they can be very different from their GR counterpart. Things can be more interesting when spontaneous scalarization kicks in. The universal relations in GR can be EOS dependent for those theories

with spontaneous scalarization, because in general, the starting point of the spontaneous scalarization is different for different EOSs. Once a NS is spontaneously scalarized, the relations can differ from their GR counterparts largely. Thus for theories with spontaneous scalarization, we can see that the relations for different EOSs branching from the GR one from different starting points. For some theories, like the DEF theory, those different relations for different EOSs will tend to form a new universal relation different from GR when the scalarization becomes stronger. However for some theories like the massive Gauss-Bonnet theory, this may or may not happen depending on the theoretical parameters [124].

1.5.2 Massive gravity theory

From a modern particle physics perspective, the related quantum particle for gravity in GR is a massless spin-2 particle, the so-called graviton. However, massive gravity theories, which maintain the notion that gravity is propagated by a spin-2 particle but consider this particle to be massive, have aroused wide interest. Such a massive gravity theory may be used to explain the acceleration of the Universe and dark matter [52]. Probing the upper limit of the graviton mass is a basic topic in physics. Constraints from the pulsar timing technique may come from two aspects: one is the radiative tests from binary pulsars, and the other is the orbital motion of a pulsar-supermassive BH system.

Unlike the dispersion relation tests from the LIGO/Virgo/KAGRA GW events [2], the constraints on the graviton mass are generally theory dependent in pulsar timing, therefore we shall introduce some specific massive gravity theories. One of the examples is the cubic Galileon theory, which is a simple model with the Vainshtein screening mechanism [31]. The action including matter is

$$S = \int \mathrm{d}^4x \left[-\frac{1}{4} h^{\mu\nu} (\mathscr{E} h)_{\mu\nu} + \frac{h^{\mu\nu} T_{\mu\nu}}{2M_{\rm Pl}} - \frac{3}{4} (\partial \pi_s)^2 \left(1 + \frac{1}{3\Lambda^3} \Box \pi_s \right) + \frac{\pi_s T}{2M_{\rm Pl}} \right], \tag{1.56}$$

where $h_{\mu\nu} = g_{\mu\nu} - \eta_{\mu\nu}$, $(\mathscr{E} h)_{\mu\nu} = -\frac{1}{2}\Box h_{\mu\nu} + \cdots$ and T is the trace of the stress-energy tensor. In the action, $M_{\rm Pl}$ is the Planck mass, and the strong coupling scale of the Galileon sector Λ is related to the graviton mass m_g via $\Lambda^3 = m_g^2 M_{\rm Pl}$. The field equation for π_s and $h_{\mu\nu}$ are [31]

$$\frac{1}{M_{\rm Pl}} T_{\mu\nu} = -\frac{1}{2} \Box h_{\mu\nu}, \tag{1.57}$$

$$\frac{1}{2M_{\rm Pl}} T = \partial_\mu \left[-\frac{3}{2} \partial^\mu \pi_s \left(1 + \frac{1}{3\Lambda^3} \Box \pi_s \right) + \frac{1}{4\Lambda^3} \partial^\mu (\partial \pi_s)^2 \right]. \tag{1.58}$$

For a static point source with mass M, the solution for π can be written as $\nabla \pi_s(r) = \hat{r} E(r)$, where

$$E_{\pm}(r) = \frac{\Lambda^3}{4r}\left[\pm\sqrt{9r^4 + \frac{32}{\pi}r_\star^3 r} - 3r^2\right], \tag{1.59}$$

and the Vainshtein radius associated with the mass M is $r_\star = \left(M/16\Lambda^3 M_{\rm pl}\right)^{1/3} = \left(M/16m_g^2 M_{\rm pl}^2\right)^{1/3}$. Within the radius $r_\star$, the fifth force from the scalar field is strongly suppressed, and the theory reduces to the canonical gravity. With such a screening mechanism, this theory can avoid the stringent constraints from the Solar system while it still can deviate from GR at a large scale, thus providing changes to the cosmological evolution.

Though the screening mechanism tends to suppress the deviation from GR at high-density regions, the cubic Galileon theory still predicts difference in gravitational radiation [31]. For a binary system with a characteristic velocity v, the gravitational radiation is less suppressed by a factor of $\sim v^{3/2}$ compared with its fifth-force counterpart. As shown by de Rham et al. [31], the extra radiative channels in these theories include monopolar radiation, dipolar radiation and quadrupolar radiation, and for different systems, for example binary pulsar systems with different orbital periods and orbital eccentricities, the dominate radiation channel can be different [101]. Recent study with 14 well-timed binary pulsar systems has set a tight constraint on the graviton mass in the cubic Galileon theory, $m_g < 2\times10^{-28}\,{\rm eV/c^2}$, at 95% confidence level [101].

Another example we discuss here is the so-called Yukawa gravity, which is a widely used phenomenological form that contains the possible deviations from the Newtonian gravity via a modified potential,

$$\Phi(r) = -\frac{GM}{(1+\alpha)r}\left(1+\alpha e^{-r/\Lambda_{\rm Y}}\right). \tag{1.60}$$

Part of the Newtonian potential is suppressed exponentially, with a strength of α and a length scale of $\Lambda_{\rm Y}$. For $\alpha = 0$ or $\Lambda_{\rm Y} = \infty$, the Yukawa potential will reduce to the Newtonian one, and the graviton mass here can be expressed as $m_g = h/\Lambda_{\rm Y}$. Such a Yukawa gravity can naturally arise in the Newtonian limit of $f(R)$ gravity with a general action [17]

$$S = \int {\rm d}^4x\sqrt{-g}\left[f(R) + \frac{16\pi G}{c^4}\mathscr{L}_m\right]. \tag{1.61}$$

Assuming that the function $f(R)$ is Taylor expandable and take the $O(2)$ approximation, $f(R) = f_0 + f_1 R + f_2 R^2 + \cdots$ with constants f_i $(i = 1,2,3)$, the gravitational potential defined via $g_{tt} = 1 + 2\Phi$ will take the form of Eq. (1.60), and the Newtonian potential is obtained only when $f(R) = f_1 R$.

Tests of the Yukawa gravity have been carried out at a wide range of length scales with different systems and methods, including terrestrial laboratory experiments [83], LAser GEOdynamic Satellite (LAGEOS) [85], Lunar Laser Ranging (LLR) [119], Solar system planetary orbits [107], S2 star orbit [129] and observations of elliptical galaxies [82]. The reason for taking experiments at such a wide

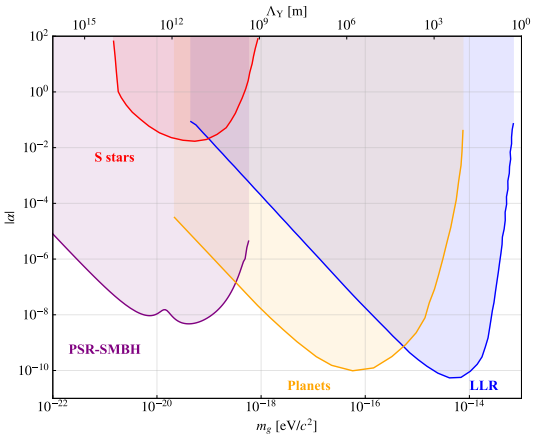

Fig. 1.8: Constraints on the strength of the Yukawa interaction α as a function of the graviton mass m_g from different experiments (figure courtesy of Y. Dong) [36]. Shaded regions show the excluded parameter space at the 95% confidence level.

coverage is that for the Yukawa gravity theory, only when the system scale L is similar to the length scale Λ_Y it shows the largest deviation from Newtonian gravity. Thus timing a pulsar orbiting around the supermassive BH in our galaxy center may provide a unique opportunity to test the Yukawa gravity theory at a new length scale [36]. For a pulsar orbit with a semi-major axis a and an orbital eccentricity e, it will experience an additional periastron advance from the Yukawa potential at the rate of [128]

$$\dot{\omega} = \frac{1}{P_b} \frac{\pi\alpha\sqrt{1-e^2}}{1+\alpha} \frac{a^2}{\Lambda_Y^2}, \tag{1.62}$$

to the first order in a/Λ_Y. If the pulsar orbit has a semi-major axis $a \sim \Lambda_Y$, periodic effects such as the deformation of the orbit may also be detectable by pulsar timing.

Figure 1.8 shows the projected constraints from a S2-like like pulsar, on the strength α at 95% confidence level as a function of m_g [36], from where one can see that the pulsar-supermassive BH system can contribute a unique test of this theory that is not covered by other experiments. For a given strength of the Yukawa interaction α one also can obtain the related constraint on the graviton mass, and from Eq. (1.62) one can see that for α changing from 1 to ∞, the periastron advance rate only changes by a factor of 2, thus the constraints on m_g will not change too much. Simulation results by Dong et al. [36] showed that the expected constraints on graviton mass can reach $m_g \lesssim 10^{-24}\,\mathrm{eV/c^2}$ for a 20-yr observation of a S2-like pulsar around Sagittarius A*.

1.6 Summary

In this chapter, we present a pedagogical introduction to some basic aspects of pulsar timing and using it in testing gravity theories. As pulsar timing provides very high accurate measurements of a strongly self-gravitating object in orbit, it can put strict constraints in the strong-field region of gravity. Moreover, the observational precision of the pulsar-timing parameters generally improves with the observational time span $T_{\rm obs}$. For example, the precision in the orbital decay parameter, $\dot{P}_b$, improves as $T_{\rm obs}^{-5/2}$. Thus long-term observations of interesting systems like the Hulse-Taylor pulsar and the double pulsar can provide us with new results from time to time until the precision is dominated by other effects (e.g. the Galactic potential model). Furthermore, the sensitivity of radio telescope is improving at the same time, so the real improvement of timing parameters is faster than the theoretical power law predictions. New telescopes like the FAST telescope in China [74] and the next-generation radio telescope, the Square Kilometre Array in South Africa and Australia [116] can provide plenty of new results. New systems like pulsar-BH binaries or pulsars near the Galactic center may be discovered, and they may lead to new tests of gravity and give better results [71, 69, 98].

As we mentioned in the chapter, combining pulsar timing observation with other observations can probe a large theory space of both gravity theories and nuclear physics. GW observations [2] and BH shadows [3] all provide unique information of gravity in different gravity regimes. For GWs, with the third generation of detectors that are under construction, almost all binary NS mergers in the Universe can be detected, and the BH shadows and X-ray tests provide the possibility of measuring the BH metric in the near zone. Combining with proper universal relations, one can break the degeneracy between gravity theories and nuclear physics, thus giving EOS-unbiased tests of gravity.

Acknowledgements We thank Yiming Dong and Yong Gao for providing figures. This work was supported by the National SKA Program of China (2020SKA0120300), the National Natural Science Foundation of China (11975027, 11991053, 12203072), and the Max Planck Partner Group Program funded by the Max Planck Society. X.M. is supported by the FAST Postdoctoral Fellowship at the National Astronomical Observatories, Chinese Academy of Sciences.

References

1. B. P. Abbott et al. GW170817: Observation of Gravitational Waves from a Binary Neutron Star Inspiral. *Phys. Rev. Lett.*, 119(16):161101, 2017.
2. R. Abbott et al. Tests of General Relativity with GWTC-3. *arXiv e-prints*, page arXiv:2112.06861, 2021.
3. K. Akiyama et al. First Sagittarius A* Event Horizon Telescope Results. VI. Testing the Black Hole Metric. *Astrophys. J. Lett.*, 930(2):L17, 2022.
4. J. Antoniadis et al. A Massive Pulsar in a Compact Relativistic Binary. *Science*, 340:6131, 2013.

5. A. M. Archibald, N. V. Gusinskaia, J. W. T. Hessels, A. T. Deller, D. L. Kaplan, D. R. Lorimer, R. S. Lynch, S. M. Ransom, and I. H. Stairs. Universality of Free Fall from the Orbital Motion of a Pulsar in a Stellar Triple System. *Nature*, 559(7712):73–76, 2018.
6. D. C. Backer. Pulsar Nulling Phenomena. *Nature*, 228(5266):42–43, 1970.
7. M. Bagchi. Prospects of Constraining the Dense Matter Equation of State from Timing Analysis of Pulsars in Double Neutron Star Binaries: The Cases of PSR J0737-3039A and PSR J1757-1854. *Universe*, 4(2):36, 2018.
8. N. Bartel, D. Morris, W. Sieber, and T. H. Hankins. The Mode-Switching Phenomenon in Pulsars. *Astrophys. J.*, 258:776–789, 1982.
9. A. Bauswein and N. Stergioulas. Semi-Analytic Derivation of the Threshold Mass for Prompt Collapse in Binary Neutron Star Mergers. *MNRAS*, 471(4):4956–4965, 2017.
10. E. Berti et al. Testing General Relativity with Present and Future Astrophysical Observations. *Class. Quant. Grav.*, 32:243001, 2015.
11. B. Bertotti, L. Iess, and P. Tortora. A Test of General Relativity Using Radio Links with the Cassini Spacecraft. *Nature*, 425:374–376, 2003.
12. R. Blandford and S. A. Teukolsky. Arrival-Time Analysis for a Pulsar in a Binary System. *Astrophys. J.*, 205:580–591, 1976.
13. H. Bondi. Massive Spheres in General Relativity. *Proc. Roy. Soc. Lond. A*, 282:303–317, 1964.
14. C. Brans and R. H. Dicke. Mach's Principle and a Relativistic Theory of Gravitation. *Phys. Rev.*, 124:925–935, 1961.
15. R. P. Breton, V. M. Kaspi, M. Kramer, M. A. McLaughlin, M. Lyutikov, S. M. Ransom, I. H. Stairs, R. D. Ferdman, F. Camilo, and A. Possenti. Relativistic Spin Precession in the Double Pulsar. *Science*, 321:104–107, 2008.
16. M. Burgay et al. An Increased Estimate of the Merger Rate of Double Neutron Stars From Observations of a Highly Relativistic System. *Nature*, 426:531–533, 2003.
17. S. Capozziello, A. Stabile, and A. Troisi. A General Solution in the Newtonian Limit of f(R)-Gravity. *Mod. Phys. Lett. A*, 24:659–665, 2009.
18. K. Chatziioannou, K. Yagi, and N. Yunes. Toward Realistic and Practical No-Hair Relations for Neutron Stars in the Nonrelativistic Limit. *Phys. Rev. D*, 90(6):064030, 2014.
19. T. Clifton, P. G. Ferreira, A. Padilla, and C. Skordis. Modified Gravity and Cosmology. *Phys. Rept.*, 513:1–189, 2012.
20. J. M. Cordes and T. J. W. Lazio. NE2001. 1. A New Model for the Galactic Distribution of Free Electrons and its Fluctuations. *arXiv e-prints*, pages astro–ph/0207156, 2002.
21. J. M. Cordes, J. M. Weisberg, and T. H. Hankins. Quasiperiodic Microstructure in Radio Pulsar Emission. *Astron. J.*, 100:1882, 1990.
22. T. Damour. Binary Systems as Test-Beds of Gravity Theories. In *6th SIGRAV Graduate School in Contemporary Relativity and Gravitational Physics: A Century from Einstein Relativity: Probing Gravity Theories in Binary Systems*, 2007.
23. T. Damour and N. Deruelle. General Relativistic Celestial Mechanics of Binary Systems. I. The Post-Newtonian Motion. *Ann. Inst. H. Poincaré Phys. Théor.*, 43(1):107–132, 1985.
24. T. Damour and N. Deruelle. General Relativistic Celestial Mechanics of Binary Systems. II. The Post-Newtonian Timing Formula. *Ann. Inst. H. Poincaré Phys. Théor.*, 44(3):263–292, 1986.
25. T. Damour and G. Esposito-Farèse. Tensor Multiscalar Theories of Gravitation. *Class. Quant. Grav.*, 9:2093–2176, 1992.
26. T. Damour and G. Esposito-Farèse. Nonperturbative Strong Field Effects in Tensor-scalar Theories of Gravitation. *Phys. Rev. Lett.*, 70:2220–2223, 1993.
27. T. Damour and G. Esposito-Farèse. Tensor-scalar Gravity and Binary Pulsar Experiments. *Phys. Rev. D*, 54:1474–1491, 1996.
28. T. Damour and A. Nagar. Relativistic Tidal Properties of Neutron Stars. *Phys. Rev. D*, 80:084035, 2009.
29. T. Damour and G. Schaefer. Higher Order Relativistic Periastron Advances and Binary Pulsars. *Nuovo Cim. B*, 101:127, 1988.

30. T. Damour and J. H. Taylor. Strong Field Tests of Relativistic Gravity and Binary Pulsars. *Phys. Rev. D*, 45:1840–1868, 1992.
31. C. de Rham, A. J. Tolley, and D. H. Wesley. Vainshtein Mechanism in Binary Pulsars. *Phys. Rev. D*, 87(4):044025, 2013.
32. G. Desvignes, M. Kramer, K. Lee, J. van Leeuwen, I. Stairs, A. Jessner, I. Cognard, L. Kasian, A. Lyne, and B. W. Stappers. Radio Emission from a Pulsar's Magnetic Pole Revealed by General Relativity. *Science*, 365(6457):1013–1017, 2019.
33. T. Dietrich, M. W. Coughlin, P. T. H. Pang, M. Bulla, J. Heinzel, L. Issa, I. Tews, and S. Antier. Multimessenger Constraints on the Neutron-Star Equation of State and the Hubble Constant. *Science*, 370(6523):1450–1453, 2020.
34. D. D. Doneva, F. M. Ramazanoğlu, H. O. Silva, T. P. Sotiriou, and S. S. Yazadjiev. Scalarization. *arXiv e-prints*, page arXiv:2211.01766, 2022.
35. D. D. Doneva and S. S. Yazadjiev. New Gauss-Bonnet Black Holes with Curvature-Induced Scalarization in Extended Scalar-Tensor Theories. *Phys. Rev. Lett.*, 120(13):131103, 2018.
36. Y. Dong, L. Shao, Z. Hu, X. Miao, and Z. Wang. Prospects for Constraining the Yukawa Gravity with Pulsars Around Sagittarius A*. *JCAP*, 11:051, 2022.
37. F. D. Drake and H. D. Craft. Second Periodic Pulsation in Pulsars. *Nature*, 220(5164):231–235, 1968.
38. R. D. Ferdman et al. The Double Pulsar: Evidence for Neutron Star Formation without an Iron Core-Collapse Supernova. *Astrophys. J.*, 767:85, 2013.
39. E. Fonseca et al. Refined Mass and Geometric Measurements of the High-Mass PSR J0740+6620. *Astrophys. J. Lett.*, 915(1):L12, 2021.
40. E. S. Fradkin and A. A. Tseytlin. Quantum String Theory Effective Action. *Nucl. Phys. B*, 269:745, 1986.
41. P. C. C. Freire and N. Wex. The Orthometric Parameterisation of the Shapiro Delay and an Improved Test of General Relativity with Binary Pulsars. *MNRAS*, 409:199, 2010.
42. P. C. C. Freire, N. Wex, G. Esposito-Farèse, J. P. W. Verbiest, M. Bailes, B. A. Jacoby, M. Kramer, I. H. Stairs, J. Antoniadis, and G. H. Janssen. The Relativistic Pulsar-White Dwarf Binary PSR J1738+0333 II. The Most Stringent Test of Scalar-Tensor Gravity. *MNRAS*, 423:3328, 2012.
43. Y. Gao, X. Lai, L. Shao, and R. Xu. Rotation and Deformation of Strangeon Stars in the Lennard-Jones Model. *MNRAS*, 509(2):2758–2779, 2021.
44. Y. Gao, L. Shao, and J. Steinhoff. A tight universal relation between the shape eccentricity and the moment of inertia for rotating neutron stars. *arXiv e-prints*, page arXiv:2303.14130, Mar. 2023.
45. T. Gold. Rotating Neutron Stars as the Origin of the Pulsating Radio Sources. *Nature*, 218:731–732, 1968.
46. M. Guo, J. Zhao, and L. Shao. Extended reduced-order surrogate models for scalar-tensor gravity in the strong field and applications to binary pulsars and gravitational waves. *Phys. Rev. D*, 104(10):104065, 2021.
47. M. Hadzic and Z. Lin. Turning Point Principle for Relativistic Stars. *Commun. Math. Phys.*, 387(2):729–759, 2021.
48. T. H. Hankins, J. S. Kern, J. C. Weatherall, and J. A. Eilek. Nanosecond Radio Bursts from Strong Plasma Turbulence in the Crab Pulsar. *Nature*, 422(6928):141–143, 2003.
49. J. B. Hartle. Slowly Rotating Relativistic Stars. I. Equations of Structure. *Astrophys. J.*, 150:1005–1029, 1967.
50. A. Hewish, S. J. Bell, J. D. H. Pilkington, P. F. Scott, and R. A. Collins. Observation of a Rapidly Pulsating Radio Source. *Nature*, 217:709–713, 1968.
51. T. Hinderer. Tidal Love Numbers of Neutron Stars. *Astrophys. J.*, 677:1216–1220, 2008.
52. K. Hinterbichler. Theoretical Aspects of Massive Gravity. *Rev. Mod. Phys.*, 84:671–710, 2012.
53. G. Hobbs. Developing a Pulsar-Based Time Standard. *Highlights Astron.*, 16:207–208, 2015.
54. H. Hu, M. Kramer, N. Wex, D. J. Champion, and M. S. Kehl. Constraining the Dense Matter Equation-of-State with Radio Pulsars. *MNRAS*, 497(3):3118–3130, 2020.

55. Z. Hu, Y. Gao, R. Xu, and L. Shao. Scalarized Neutron Stars in Massive Scalar-Tensor Gravity: X-ray Pulsars and Tidal Deformability. *Phys. Rev. D*, 104(10):104014, 2021.
56. R. A. Hulse and J. H. Taylor. Discovery of a Pulsar in a Binary System. *Astrophys. J. Lett.*, 195:L51–L53, 1975.
57. B. Jain and J. Khoury. Cosmological Tests of Gravity. *Annals Phys.*, 325:1479–1516, 2010.
58. M. Kramer. New Results from Testing Relativistic Gravity with Radio Pulsars. *Int. J. Mod. Phys. D*, 31(06):2230010, 2022.
59. M. Kramer et al. Tests of General Relativity from Timing the Double Pulsar. *Science*, 314:97–102, 2006.
60. M. Kramer et al. Strong-Field Gravity Tests with the Double Pulsar. *Phys. Rev. X*, 11(4):041050, 2021.
61. M. Kramer and N. Wex. The Double Pulsar System: A Unique Laboratory for Gravity. *Class. Quant. Grav.*, 26:073001, 2009.
62. D. Lai, F. A. Rasio, and S. L. Shapiro. Ellipsoidal Figures of Equilibrium-Compressible Models. *Astrophys. J. Suppl.*, 88:205–252, 1993.
63. X. Lai and R. Xu. Strangeon and Strangeon Star. *J. Phys. Conf. Ser.*, 861(1):012027, 2017.
64. P. Landry and B. Kumar. Constraints on the Moment of Inertia of PSR J0737-3039A from GW170817. *Astrophys. J. Lett.*, 868(2):L22, 2018.
65. J. M. Lattimer. Neutron Star Mass and Radius Measurements. *Universe*, 5(7):159, 2019.
66. J. M. Lattimer and M. Prakash. Neutron Star Structure and the Equation of State. *Astrophys. J.*, 550:426, 2001.
67. H. Li, Y. Gao, L. Shao, R. Xu, and R. Xu. Oscillation Modes and Gravitational Waves from Strangeon Stars. *MNRAS*, 516(4):6172–6179, 2022.
68. L. Lindblom. Determining the Nuclear Equation of State from Neutron-Star Masses and Radii. *Astrophys. J.*, 398:569–573, 1992.
69. K. Liu, R. P. Eatough, N. Wex, and M. Kramer. Pulsar–Black Hole Binaries: Prospects for New Gravity Tests with Future Radio Telescopes. *MNRAS*, 445(3):3115–3132, 2014.
70. K. Liu et al. Variability, polarimetry, and timing properties of single pulses from PSR J1713+0747 using the Large European Array for Pulsars. *Mon. Not. Roy. Astron. Soc.*, 463(3):3239–3248, 2016.
71. K. Liu, N. Wex, M. Kramer, J. M. Cordes, and T. J. W. Lazio. Prospects for Probing the Spacetime of Sgr A* with Pulsars. *Astrophys. J.*, 747:1, 2012.
72. D. R. Lorimer. Binary and Millisecond Pulsars. *Living Rev. Rel.*, 8:7, 2005.
73. D. R. Lorimer and M. Kramer. *Handbook of Pulsar Astronomy*. Cambridge University Press, 2005.
74. J. Lu, K. Lee, and R. Xu. Advancing Pulsar Science with the FAST. *Sci. China Phys. Mech. Astron.*, 63(2):229531, 2020.
75. S. C. Lundgren, J. M. Cordes, M. Ulmer, S. M. Matz, S. Lomatch, R. S. Foster, and T. Hankins. Giant Pulses from the Crab Pulsar: A Joint Radio and Gamma-Ray Study. *Astrophys. J.*, 453:433, 1995.
76. A. G. Lyne et al. A Double-Pulsar System: A Rare Laboratory for Relativistic Gravity and Plasma Physics. *Science*, 303:1153–1157, 2004.
77. R. Malhotra, D. Black, A. Eck, and A. Jackson. Resonant Orbital Evolution in the Putative Planetary System of PSR1257+12. *Nature*, 356(6370):583–585, 1992.
78. R. N. Manchester. Pulsars and Gravity. *Int. J. Mod. Phys. D*, 24(06):1530018, 2015.
79. R. N. Manchester, G. B. Hobbs, A. Teoh, and M. Hobbs. The Australia Telescope National Facility Pulsar Catalogue. *Astron. J.*, 129:1993, 2005.
80. R. F. P. Mendes and N. Ortiz. Highly Compact Neutron Stars in Scalar-Tensor Theories of Gravity: Spontaneous Scalarization versus Gravitational Collapse. *Phys. Rev. D*, 93(12):124035, 2016.
81. M. C. Miller et al. PSR J0030+0451 Mass and Radius from *NICER* Data and Implications for the Properties of Neutron Star Matter. *Astrophys. J. Lett.*, 887(1):L24, 2019.
82. N. R. Napolitano, S. Capozziello, A. J. Romanowsky, M. Capaccioli, and C. Tortora. Testing Yukawa-Like Potentials From f(R)-Gravity in Elliptical Galaxies. *Astrophys. J.*, 748:87, 2012.

83. T. M. Niebauer, M. P. Mchugh, and J. E. Faller. Galilean Test for the Fifth Force. *Phys. Rev. Lett.*, 59:609–612, 1987.
84. J. R. Oppenheimer and G. M. Volkoff. On Massive Neutron Cores. *Phys. Rev.*, 55:374–381, 1939.
85. R. Peron. Testing General Relativistic Predictions with the LAGEOS Satellites. *Adv. High Energy Phys.*, 2014:791367, 2014.
86. F. M. Ramazanoğlu and F. Pretorius. Spontaneous Scalarization with Massive Fields. *Phys. Rev. D*, 93(6):064005, 2016.
87. S. M. Ransom et al. A millisecond pulsar in a stellar triple system. *Nature*, 505:520, 2014.
88. R. D. Reasenberg, I. I. Shapiro, P. E. MacNeil, R. B. Goldstein, J. C. Breidenthal, J. P. Brenkle, D. L. Cain, T. M. Kaufman, T. A. Komarek, and A. I. Zygielbaum. Viking relativity experiment: Verification of signal retardation by solar gravity. *Astrophys. J. Lett.*, 234:L219–L221, 1979.
89. B. Reina. Slowly Rotating Homogeneous Masses Revisited. *MNRAS*, 455(4):4512–4517, 2016.
90. T. E. Riley et al. A *NICER* View of PSR J0030+0451: Millisecond Pulsar Parameter Estimation. *Astrophys. J. Lett.*, 887(1):L21, 2019.
91. D. S. Robertson, W. E. Carter, and W. H. Dillinger. New Measurement of Solar Gravitational Deflection of Radio Signals Using VLBI. *Nature*, 349(6312):768–770, 1991.
92. A. Saffer and K. Yagi. Tidal Deformabilities of Neutron Stars in Scalar-Gauss-Bonnet Gravity and their Applications to Multimessenger Tests of Gravity. *Phys. Rev. D*, 104(12):124052, 2021.
93. B. S. Sathyaprakash et al. Extreme gravity and fundamental physics. *Bull. Am. Astron. Soc.*, 51(3):251, May 2019.
94. N. Sennett, L. Shao, and J. Steinhoff. Effective action model of dynamically scalarizing binary neutron stars. *Phys. Rev. D*, 96(8):084019, 2017.
95. R. M. Shannon and J. M. Cordes. Pulse intensity modulation and the timing stability of millisecond pulsars: A case study of PSR J1713+0747. *Astrophys. J.*, 761:64, 2012.
96. L. Shao. Degeneracy in Studying the Supranuclear Equation of State and Modified Gravity with Neutron Stars. *AIP Conf. Proc.*, 2127(1):020016, 2019.
97. L. Shao. Radio Pulsars as a Laboratory for Strong-field Gravity Tests. *arXiv e-prints*, page arXiv:2206.15187, 2022.
98. L. Shao et al. Testing Gravity with Pulsars in the SKA Era. *PoS*, AASKA14:042, 2015.
99. L. Shao, N. Sennett, A. Buonanno, M. Kramer, and N. Wex. Constraining Nonperturbative Strong-Field Effects in Scalar-Tensor Gravity by Combining Pulsar Timing and Laser-Interferometer Gravitational-Wave Detectors. *Phys. Rev. X*, 7(4):041025, 2017.
100. L. Shao and N. Wex. Tests of Gravitational Symmetries with Radio Pulsars. *Sci. China Phys. Mech. Astron.*, 59(9):699501, 2016.
101. L. Shao, N. Wex, and S. Zhou. New Graviton Mass Bound from Binary Pulsars. *Phys. Rev. D*, 102(2):024069, 2020.
102. L. Shao and K. Yagi. Neutron Stars as Extreme Laboratories for Gravity Tests. *Sci. Bull.*, 67:1946–1949, 2022.
103. H. O. Silva, A. M. Holgado, A. Cárdenas-Avendaño, and N. Yunes. Astrophysical and Theoretical Physics Implications from Multimessenger Neutron Star Observations. *Phys. Rev. Lett.*, 126(18):181101, 2021.
104. H. O. Silva, J. Sakstein, L. Gualtieri, T. P. Sotiriou, and E. Berti. Spontaneous Scalarization of Black Holes and Compact Stars from a Gauss-Bonnet Coupling. *Phys. Rev. Lett.*, 120(13):131104, 2018.
105. D. H. Staelin and I. Reifenstein, Edward C. Pulsating Radio Sources near the Crab Nebula. *Science*, 162(3861):1481–1483, 1968.
106. I. H. Stairs. Testing General Relativity with Pulsar Timing. *Living Rev. Rel.*, 6:5, 2003.
107. C. Talmadge, J. P. Berthias, R. W. Hellings, and E. M. Standish. Model Independent Constraints on Possible Modifications of Newtonian Gravity. *Phys. Rev. Lett.*, 61:1159–1162, 1988.

108. T. M. Tauris et al. Formation of Double Neutron Star Systems. *Astrophys. J.*, 846(2):170, 2017.
109. J. H. Taylor, L. A. Fowler, and P. M. McCulloch. Measurements of General Relativistic Effects in the Binary Pulsar PSR 1913+16. *Nature*, 277:437–440, 1979.
110. R. C. Tolman. Static Solutions of Einstein's Field Equations for Spheres of Fluid. *Phys. Rev.*, 55:364–373, 1939.
111. G. Voisin, I. Cognard, P. C. C. Freire, N. Wex, L. Guillemot, G. Desvignes, M. Kramer, and G. Theureau. An improved test of the strong equivalence principle with the pulsar in a triple star system. *Astron. Astrophys.*, 638:A24, 2020.
112. N. Wang, R. N. Manchester, and S. Johnston. Pulsar Nulling and Mode Changing. *MNRAS*, 377:1383–1392, 2007.
113. S. Weinberg. On the Development of Effective Field Theory. *Eur. Phys. J. H*, 46(1):6, 2021.
114. J. M. Weisberg and Y. Huang. Relativistic Measurements from Timing the Binary Pulsar PSR B1913+16. *Astrophys. J.*, 829(1):55, 2016.
115. P. Weltevrede, R. T. Edwards, and B. W. Stappers. The Subpulse Modulation Properties of Pulsars at 21 cm. *Astron. Astrophys.*, 445:243, 2006.
116. A. Weltman et al. Fundamental Physics with the Square Kilometre Array. *Publ. Astron. Soc. Austral.*, 37:e002, 2020.
117. N. Wex. Testing Relativistic Gravity with Radio Pulsars. In S. M. Kopeikin, editor, *Frontiers in Relativistic Celestial Mechanics: Applications and Experiments*, volume 2, page 39. Walter de Gruyter GmbH, Berlin/Boston, 2014.
118. C. M. Will. *Theory and Experiment in Gravitational Physics*. Cambridge University Press, 2018.
119. J. G. Williams, S. G. Turyshev, and D. H. Boggs. Lunar laser Ranging Tests of the Equivalence Principle with the Earth and Moon. *Int. J. Mod. Phys. D*, 18:1129–1175, 2009.
120. E. Witten. Cosmic Separation of Phases. *Phys. Rev. D*, 30:272–285, 1984.
121. A. Wolszczan and D. A. Frail. A Planetary system around the millisecond pulsar PSR 1257+12. *Nature*, 355:145–147, 1992.
122. R. Xu. Solid Quark Matter? *Astrophys. J. Lett.*, 596:L59–L62, 2003.
123. R. Xu, Y. Gao, and L. Shao. Strong-Field Effects in Massive Scalar-Tensor Gravity for Slowly Spinning Neutron Stars and Application to X-ray Pulsar Pulse Profiles. *Phys. Rev. D*, 102(6):064057, 2020.
124. R. Xu, Y. Gao, and L. Shao. Neutron Stars in Massive Scalar-Gauss-Bonnet Gravity: Spherical Structure and Time-Independent Perturbations. *Phys. Rev. D*, 105(2):024003, 2022.
125. K. Yagi and N. Yunes. I-Love-Q Relations in Neutron Stars and their Applications to Astrophysics, Gravitational Waves and Fundamental Physics. *Phys. Rev. D*, 88(2):023009, 2013.
126. K. Yagi and N. Yunes. Approximate Universal Relations for Neutron Stars and Quark Stars. *Phys. Rept.*, 681:1–72, 2017.
127. J. M. Yao, R. N. Manchester, and N. Wang. A New Electron-density Model for Estimation of Pulsar and FRB Distances. *Astrophys. J.*, 835(1):29.
128. A. F. Zakharov, P. Jovanović, D. Borka, and V. Borka Jovanović. Constraining the Range of Yukawa Gravity Interaction from S2 Star Orbits III: Improvement Expectations for Graviton Mass Bounds. *JCAP*, 04:050, 2018.
129. A. F. Zakharov, P. Jovanovic, D. Borka, and V. B. Jovanovic. Constraining the Range of Yukawa Gravity Interaction from S2 Star Orbits II: Bounds on Graviton Mass. *JCAP*, 05:045, 2016.
130. J. Zhao, P. C. C. Freire, M. Kramer, L. Shao, and N. Wex. Closing a Spontaneous-scalarization Window with Binary Pulsars. *Class. Quant. Grav.*, 39(11):11LT01, 2022.
131. J. Zhao, L. Shao, Z. Cao, and B.-Q. Ma. Reduced-order surrogate models for scalar-tensor gravity in the strong field regime and applications to binary pulsars and GW170817. *Phys. Rev. D*, 100(6):064034, 2019.
132. E. Zhou, K. Kiuchi, M. Shibata, A. Tsokaros, and K. Uryu. Evolution of Equal Mass Binary Bare Quark Stars in Full General Relativity: Could a Supramassive Merger Remnant Experience Prompt Collapse? *Phys. Rev. D*, 106(10):103030, 2022.
133. W. W. Zhu et al. Tests of Gravitational Symmetries with Pulsar Binary J1713+0747. *Mon. Not. Roy. Astron. Soc.*, 482(3):3249–3260, 2019.